


7-2015

# Traction-Separation Relationships for Hydrogen-Induced Grain Boundary Embrittlement in Nickel via Molecular Dynamics Simulations

Wesley Allen Barrows  
*University of Arkansas, Fayetteville*

Follow this and additional works at: <http://scholarworks.uark.edu/etd>

 Part of the [Applied Mechanics Commons](#), [Mechanics of Materials Commons](#), and the [Nanoscience and Nanotechnology Commons](#)

---

## Recommended Citation

Barrows, Wesley Allen, "Traction-Separation Relationships for Hydrogen-Induced Grain Boundary Embrittlement in Nickel via Molecular Dynamics Simulations" (2015). *Theses and Dissertations*. 1278.  
<http://scholarworks.uark.edu/etd/1278>

This Thesis is brought to you for free and open access by ScholarWorks@UARK. It has been accepted for inclusion in Theses and Dissertations by an authorized administrator of ScholarWorks@UARK. For more information, please contact [scholar@uark.edu](mailto:scholar@uark.edu), [ccmiddle@uark.edu](mailto:ccmiddle@uark.edu).

Traction-Separation Relationships for Hydrogen-Induced Grain Boundary Embrittlement in  
Nickel via Molecular Dynamics Simulations

A thesis submitted in partial fulfillment  
of the requirements for the degree of  
Master of Science in Mechanical Engineering

By

Wesley A. Barrows  
University of Arkansas  
Bachelor of Science in Mechanical Engineering, 2013  
University of Arkansas  
Bachelor of Science in Physics, 2013

July 2015  
University of Arkansas

This thesis is approved for recommendation to the Graduate Council.

---

Dr. Douglas Spearot  
Thesis Director

---

Dr. Arun Nair  
Committee Member

---

Dr. Rémi Dingreville  
Committee Member

## ABSTRACT

The deleterious effects of atomic and molecular hydrogen on the mechanical properties of metals have long been observed. Although several theories exist describing the mechanisms by which hydrogen negatively influences the failure of materials, a consensus has yet to be reached regarding the exact mechanism or combination of mechanisms. Two mechanisms have gained support in explaining hydrogen's degradative role in non-hydride forming metals: hydrogen-enhanced localized plasticity and hydrogen-enhanced decohesion. Yet, the interplay between these mechanisms and microstructure in metallic materials has not been explained. Accordingly, for this thesis, the three main objectives are: (i) to develop a numerical methodology to extract traction-separation relationships from atomistic simulation data during steady-state crack propagation along a grain boundary, building upon prior work employing atomistic cohesive zone volume elements (CZVEs); (ii) to apply the numerical methodology to specific grain boundary systems with different amounts of hydrogen located at the grain boundary interface; (iii) to further the understanding, based on the traction-separation relationships, of the mechanisms by which hydrogen effects the decohesion of a grain boundary system. A range of  $\langle 110 \rangle$  symmetric tilt grain boundaries in Ni are studied, with hydrogen coverages and favorable sites for hydrogen segregation motivated by Monte Carlo calculations. A sensitivity analysis is performed on the CZVE approach, clarifying the role of CZVE size and numerical parameters necessary to differentiate elastic and decohesion data. Results show that increasing hydrogen coverage can asymmetrically influence crack tip velocity during propagation, leads to a general decrease in the work of separation and promotes a reduction in the peak stress in the extracted traction-separation relationships, though these trends are dependent on the grain boundary structures.

## ACKNOWLEDGMENT

This research is supported by the Laboratory Directed Research and Development program at Sandia National Laboratories, a multi-program laboratory managed and operated by Sandia corporation, a wholly owned subsidiary of Lockheed Martin Corporation, for the U.S. Department of Energy's National Nuclear Security Administration under contract DE-AC04-94AL85000. Simulations were performed at the Arkansas High Performance Computing Center, supported in part by the National Science Foundation under grants MRI #0722625, MRI-R2 #0959124, and #0918970.

## TABLE OF CONTENTS

CHAPTER 1: INTRODUCTION .....	1
1.1 Hydrogen Embrittlement .....	1
1.1.1 Stress-Induced Hydride Formation .....	1
1.1.2 Hydrogen-Induced Decohesion (HID) .....	4
1.1.3 Hydrogen-Enhanced Localized Plasticity (HELP).....	7
1.1.4 Theory of Coexistent HID and HELP .....	8
1.2 Traction-Separation Relationships .....	10
1.2.1 Classical Needleman Type Formulations.....	11
1.2.2 Efforts to Derive Traction-Separation Relationships .....	12
1.3 Thesis Objectives and Structure .....	13
1.4 References .....	15
CHAPTER 2: BACKGROUND.....	20
2.1 Atomistic Simulations .....	20
2.2 Interatomic Potential .....	23
2.2.1 Introduction .....	23
2.2.2 Ni-H Interatomic Potential .....	24
2.3 Monte Carlo Simulations.....	25
2.4 Molecular Statics Simulations.....	26
2.5 Molecular Dynamics Simulations .....	26
2.5.1 Initializing the System.....	27
2.5.2 Thermodynamic State of the System.....	28
2.5.3 Velocity Verlet Integration Technique.....	30
2.6 References .....	30

CHAPTER 3: IMPLEMENTATION AND APPLICATION OF THE ATOMISTIC COHESIVE ZONE VOLUME ELEMENT APPROACH TO THE LATERAL TWIN GRAIN BOUNDARY SYSTEM.....	32
3.1 Steady-State Crack Propagation Simulation Model.....	32
3.1.1 Creation of Hydrogenated Grain Boundaries.....	32
3.1.2 Steady-State Crack Propagation.....	36
3.2 Extraction of Traction-Separation Behavior.....	37
3.2.1 Definition of Cohesive Zone Volume Elements (CZVE).....	37
3.2.2 Deconvolution of Elastic and Decohesion Response.....	39
3.2.3 Influence of Averaging Scheme on Traction-Separation.....	43
3.3 Role of H on Intergranular Embrittlement.....	45
3.3.1 Crack Tip Plasticity.....	45
3.3.2 Decohesion Behavior.....	46
3.4 References.....	51
CHAPTER 4: APPLICATION OF THE ATOMISTIC COHESIVE ZONE VOLUME ELEMENT APPROACH TO GRAIN BOUNDARIES VICINAL TO THE COHERENT TWIN.....	53
4.1 Significance of the Grain Boundaries Near to the Vicinal Twin.....	53
4.2 Creation of Hydrogenated Grain Boundary Systems.....	55
4.3 Steady-State Crack Propagation.....	56
4.4 Decohesion Behavior.....	57
4.5 References.....	65
CHAPTER 5: CONCLUSIONS.....	66
5.1 Summary.....	66
5.2 Recommendations for Future Work.....	68

## LIST OF FIGURES

Figure 1.1. (A) Schematic demonstrating film-rupture theory in which hydride formation propagates along alpha-beta interface (b) until it reaches a critical size and crack (c) leading to ductile crack propagation (d) and a repeat of the process (e-f) leading to a fracture surface (g). (B) Fracture surface showing terrace steps of alpha-beta titanium resulting from the presence of gaseous hydrogen.[2] .....	2
Figure 1.2. (A) Effect of H position ahead of crack tip on stress intensity factor. (B) Initial H (red atom) positions b (top), c (middle), d (bottom).[3].....	3
Figure 1.3. Scanning electron micrograph of steel specimen after being loaded in gaseous hydrogen and fractured in air showing the regions and fracture surface structures corresponding to the precrack, the hydrogen induced intergranular cracking, and subsequent rupture [14].....	4
Figure 1.4. Effect of dopant concentrations of Sb, Sn, and P, respectively, on $K_{IC}$ in air and $K_{TH}$ in gaseous hydrogen. [14] .....	66
Figure 1.5. Numerically predicted (solid line) and experimental (highlighted area) effect of hydrogen concentration on fracture strength , in terms of normalized nominal bending stress, for single edged-notch type specimen in four point bend test. [5] .....	6
Figure 1.6. HVEM images of strained Ni specimen in vacuum (left) and the same strained region in the presence of gaseous hydrogen at a pressure of 7kPa. [23] .....	8
Figure 1.7. TEM images of loaded Ni specimen with crack in air (left) and in gaseous hydrogen (right) . Right image taken after 30 minutes of exposure to hydrogen and clearly shows the change in dislocation behavior. [26].....	8
Figure 1.8. (A) Ni notch specimen (B) localized area of hydrogen atom placement (C) simulations at 80,000ps containing (top left) 0, (top right) 100 , (mid left) 500, (mid right) 1000, (bottom left) 2000, and (bottom right) 4122 hydrogen atoms (D) reduction in area % with respect to time for different amounts of hydrogen. [1] .....	10
Figure 1.9: Example of normal traction, $T_n$ , as a function of the normalized opening displacement, $u_n$ , where the traction and opening displacement have been normalized by the cohesive strength, $\sigma_{max}$ , and a characteristic length, $\delta$ , respectively. [34] .....	12
Figure 2.1. Two-dimensional illustration of periodic boundary conditions. [46].....	22
Figure 3.1. Schematic of the four layer crack-propagation model and cohesive zone volume element (CZVE) definition. The grain boundary between Grain 1 and Grain 2 is the primary grain boundary where the atomically sharp crack is introduced along with varying concentrations of hydrogen. The grain boundaries between Grain 1 and Absorbing Layer 2, Grain 2 and Absorbing Layer 1, and Absorbing Layer 1 and 2 all serve to ensure that dislocations emitted during crack propagation do not pass across the periodic boundaries causing the crack to interact with its own periodic image. Atoms within $h$ of the primary grain boundary are assigned to CZVEs unless they fall within $5 \text{ \AA}$ of the periodic boundary or within the region containing the atomically sharp crack, $L_{crack}$ .....	33

Figure 3.2. Structure of the primary  $\Sigma 3(112)[110]$  grain boundary. (A) and (B) Hydrogen-free minimum energy grain boundary structures colored by  $\{110\}$  atomic plane and the centrosymmetry parameter, respectively. (C) Projection along the misorientation axis and (D) rotated view of the grain boundary with H atoms (yellow) in the three most energetically favorable positions determined by Monte Carlo simulations. [42]..... 35

Figure 3.3. Traction-separation density of states,  $\rho(\sigma,\lambda)$ , for crack propagation to the left (left column) and right (right column) for a grain boundary with 25% H using 40 (row 1), 100 (row 2), 200 (row 3), and 400 (row 4) total CZVE pairs. Using 40 and 100 CZVE pairs results in data sparsely populated in some crack opening bands while using 400 CZVE pairs results in a density highly dependent on thermal vibrations, phonon wave propagation, and dislocation nucleation events. .... 40

Figure 3.4. Anatomy of the traction-separation curve. Region 1 contains states corresponding to CZVE pairs far ahead of the crack tip to be unaffected by the plasticity ahead of the crack tip or the crack tip itself. Data points in Region 2 correspond to CZVE pairs significantly affected by the plasticity ahead of the crack tip or contain the crack tip. Data points in Region 3 correspond to separated CZVE pairs through which the crack tip has passed through but have not separated completely. Data points in Region 4 correspond to CZVE pairs far behind the crack tip that have significantly separated. The screened points, shown in red, are omitted when including 2 CZVE ahead of the left crack tip with 25% H coverage at the primary grain boundary. .... 41

Figure 3.5. (A) and (B) Density of states for CZVEs located ahead of the left and right crack tips, respectively. Red data points correspond to screened elastic stiffness points when including 2 CZVE ahead of the propagating crack tips. (C) and (D) Survey of the effect of inclusion of different numbers of CZVEs ahead of propagating crack tip on the traction-separation relationship for both left (C) and right (D) crack tips for 25% H coverage at the grain boundary. All simulations are performed using 100 CZVE pairs ahead of each crack tip and plots are generated using a running averaging with  $M=250$  points..... 42

Figure 3.6. Survey of the effect of averaging methodology on the extracted traction-separation curves using filtered data for propagation of the left crack tip with 25% H coverage: (A) survey of bin size effects (B) survey of running average parameter,  $M$ , effects..... 44

Figure 3.7. Dislocation activity during crack propagation colored by the centrosymmetry parameter at 10,000 ps with (A) 0%, (B) 25%, (C) 50%, (D) 66.4%, (E) 75%, and (F) 100% H coverage at the primary grain boundary. Hydrogen saturation at the grain boundary influences both the structure of the grain boundary and dislocation nucleation during crack propagation... 46

Figure 3.8. (A) Crack tip position as a function of time. Propagation of the right crack tip is positive and propagation of the left crack tip is negative relative to the grain boundary model coordinate system, The data for 66.4% coverage corresponds to the simulation shown in Fig. 7.(B) Crack tip speed as a function of H coverage. The left and right crack tip speeds for the 66.4% coverage case are the average values of the three simulations that were performed. .... 48

Figure 4.1. Grain boundary structures for the interior (A), coherent twin (B), and exterior (C) grain boundaries. Atoms are colored by centrosymmetry, which is a measure of the perfectness of the surrounding lattice structure. In this figure, propagation to the left is in the negative x-direction and propagation to the right is in the positive x-direction. .... 54



Figure 4.2. Energetically favorable positions for H (purple) atoms to occupy within the interior (A) and exterior (B) Ni (red and blue atoms) grain boundaries. The H coverages shown correspond to the 100% saturation case. The H atoms tend to segregate to the disconnection cores (A) and stacking faults (B) . ..... 55

Figure 4.3. Dislocation activity during crack propagation colored by the centrosymmetry parameter. The top row of figures correspond to the interior grain boundary system at 20,000 ps with 0% H (A), 100% H (B) and 150% H (C) coverages at the primary grain boundary. Similarly, the bottom row of figures correspond to the exterior grain boundary system at 15,000 ps with 0% H (D), 100% H (E) and 150% H (F) coverages at the primary grain boundary. Hydrogen saturation at the grain boundary influences both the structure of the grain boundary and dislocation nucleation during crack propagation. .... 58

Figure 4.4. Traction-separation curves for crack propagation in the interior grain boundary system [left (-x direction) (A); right (+x direction) (B)] and the exterior grain boundary system [left (-x direction) (C); right (+x direction) (D)]..... 60

Figure 4.5. Dependence of the work of separation and peak stress as a function of H coverage for propagation of the (A) left (-x direction) and (B) right (+x direction) crack tips in the interior (100.52°) grain boundary system..... 62

Figure 4.6. Dependence of the work of separation and peak stress as a function of H coverage for propagation of the (A) left (-x direction) and (B) right (+x direction) crack tips in the exterior (119.6°) grain boundary system..... 63

Figure 4.7. Dependence of percentage of intergranular fracture of pure polycrystalline Ni tensile test specimen on the charged bulk hydrogen concentration at three temperatures.[60] ..... 64

LIST OF TABLES

Table 2.1. Quantities that are fitted (distinguished by \* or, if guaranteed to be correct, []) and predicted by the embedded atom method. The vacancy formation energy,  $E_f^V$ , and cohesive energy,  $E_{Coh}$ , are both in eV, the stacking fault energy,  $E^{sf}$  is in  $\text{erg}\cdot\text{cm}^{-2}$ , and the elastic constants,  $E_1^{S**}$ , are in  $10^{12} \text{ dyn}\cdot\text{cm}^{-2}$  [47]..... 24

Table 3.1. Crack tip velocity and work of separation for both crack tips at all saturation levels simulated. Crack tip velocity is determined by fitting a line to crack tip propagation data; peak stress is determined using  $M=250$  running average technique to extract traction-separation relationship; work of separation is computed using a numerical integration technique..... 51

Table 4.1. Lattice orientations used to model the interior, coherent twin, and exterior grain boundaries. The designations of Grain 1 and Grain 2 are consistent with the convention put forth in Chapter 3 in Figure 3.1. .... 53

Table 4.2. Peak stress and work of separation for both crack tips at all saturation levels simulated for the interior grain boundary. The peak stress is determined using  $M=250$  running average technique to extract traction-separation relationship and the work of separation is computed using a numerical integration technique. .... 62

Table 4.3. Peak stress and work of separation for both crack tips at all saturation levels simulated for the exterior grain boundary. The peak stress is determined using  $M=250$  running average technique to extract traction-separation relationship and the work of separation is computed using a numerical integration technique. .... 63

## LIST OF ORIGINAL ARTICLES

“Traction-Separation Relationships for Hydrogen Induced Grain Boundary Embrittlement in Nickel via Molecular Dynamics Simulations” Barrows, Wesley; Dingreville, Rémi; Spearot, Douglas.

Publication Status: Submitted for review to Modelling and Simulation in Materials Science and Engineering (MSMSE) on June 5<sup>th</sup>, 2015.

This work is reproduced in Chapter 3 and parts of Chapter 5 of this thesis.

Relevant information from Nonlinearity Assignment of Copyright Form:

### “3. Author Rights

3.1 IOPP grants the Named Authors the rights specified in 3.2 and 3.3. All such rights must be exercised for non-commercial purposes, if possible should display citation information and IOPP's copyright notice, and for electronic use best efforts must be made to include a link to the on-line abstract in the Journal. Exercise of the rights in 3.3 additionally must not use the final published IOPP format but the Named Author's own format (which may include amendments made following peer review).

#### 3.2 The rights are:

3.2.1 To make copies of the Article (all or part) for teaching purposes;

3.2.2 To include the Article (all or part) in a research thesis or dissertation;

3.2.3 To make oral presentation of the Article (all or part) and to include a summary and/or highlights of it in papers distributed at such presentations or in conference proceedings; and

3.2.4 All proprietary rights other than copyright.

#### 3.3 The additional rights are to:

3.3.1 Use the Article (all or part) without modification in personal compilations or publications of a Named Author's own works (provided not created by third party publisher);

3.3.2 Include the Article (all or part) on a Named Author's own personal web site;

3.3.3 Include the Article (all or part) on web sites of the Institution (including its repository) where a Named Author worked when research for the Article was carried out; and

3.3.4 Include the Article (all or part) on third party web sites including e-print servers, but not on other publisher's web sites.”

## IMAGE REPRODUCTION LICENSE AGREEMENTS

Figure 1.1: Springer and Metallurgical Transactions, A, Physical Metallurgy and Materials Science, 7, 1976, A film-rupture model of hydrogen-induced, slow crack growth in acicular alpha-beta titanium, H.G. Nelson, Figures 6-7, original copyright notice is given to the publication in which the material was originally published, by adding; with kind permission from Springer Science and Business Media.

Figure 1.2: Reprinted from Computational Materials Science, 69, M. Ruda, G. Bertolino, D. Farkas, A. Baruj, Effect of dilute H on crack tip plasticity in Zr, 327-334, Copyright (2013), with permission from Elsevier.

Figure 1.4: Springer and Metallurgical Transactions, A, Physical Metallurgy and Materials Science, 14, 1983, Solute segregation and hydrogen-induced intergranular fracture in an alloy steel, Jun Kameda, Figure 6, original copyright notice is given to the publication in which the material was originally published, by adding; with kind permission from Springer Science and Business Media.

Figure 1.5: Reprinted from Journal of the Mechanics and Physics of Solids, 58, P. Novak, R. Yuan, B.P. Somerday, P. Sofronis, R.O. Ritchie, A statistical, physical-based, micro-mechanical model of hydrogen-induced intergranular fracture in steel, 206-226, Copyright (2010), with permission from Elsevier.

Figure 1.6: Reprinted from Scripta Metallurgica, 15, T. Matsumoto, J. Eastman, H.K. Birnbaum, Direct observations of enhanced dislocation mobility due to hydrogen, 1033-1037, Copyright (1981), with permission from Elsevier.

Figure 1.9: Reprinted from *Journal of the mechanics and Physics of Solids*, 38, A. Needleman, An analysis of tensile decohesion along an interface, 289-324, Copyright (1990), with permission from Elsevier.

Figure 4.7: Reprinted from *Acta Metallurgica*, 34, D.H. Lassila, H.K. Birnbaum, The effect of diffusive hydrogen segregation on fracture of polycrystalline nickel, 1237-1243, Copyright (1986), with permission from Elsevier.

## CHAPTER 1: INTRODUCTION

### 1.1 Hydrogen Embrittlement

Environment assisted cracking, also known as stress corrosion cracking, is the process by which a subcritical crack grows in a material in the presence of stress and a degradative environment. Atomic species from the environment diffuse to microscopic cracks, through both interstitial and intergranular diffusion, and can cause failure at loads well below the load the material was designed to withstand. Hydrogen embrittlement refers to the case of stress corrosion cracking where hydrogen serves as the embrittling atomic species that causes a macroscopic loss of ductility, reduction in toughness, and a fracture mode transition from ductile to brittle. Embrittlement due to absorption of hydrogen is especially important because of hydrogen's high solubility and diffusivity, which make it highly potent at embrittling metals. However, the precise mechanisms by which hydrogen causes embrittlement have been the subject of considerable debate. Some of the most widely proposed and studied mechanisms include: (i) failure due to hydride formation [1–3], and in non-hydride forming metals (ii) hydrogen-enhanced localized plasticity (HELP) [4–6] and (iii) hydrogen-induced decohesion (HID) [7–9].

#### 1.1.1 Stress-Induced Hydride Formation

In metals with stable hydride phases, absorption of hydrogen can lead to localized phase changes and the formation of hydrides, which can subsequently lead to cleavage fracture. Stable hydride formation and cleavage fracture have been observed by experimental observations and predicted by thermodynamic computations in Group IV and V metals (Ti [2], Zr [3], V[10], and Nb [10,11]). The formation of hydride phases (which have a greater unit cell volume than the original material) causes strains and stresses to form at the newly formed hydride-material

interface. As the hydride region or film expands to a critical thickness, the film or region will fracture leading to cleavage or failure, as shown in Fig. 1.1(A). The stress-induced hydride formation embrittlement mechanism has been established and is not the focus of as much debate as the HELP and HID mechanisms.

An experimental study performed by Nelson [2] on acicular alpha-beta titanium alloys explored the relationship between fracture morphology and hydrogen induced crack growth. Their results showed that the width of terrace steps (Fig. 1.1(B)) on the fracture surface is inversely proportional to the rate of hydrogen-induced crack growth (which is shown to be dependent on the rate of hydride phase formation). These results were consistent with the repetitive formation and rupture of thin titanium hydride films formed in alpha-titanium at the alpha-beta titanium boundaries ahead of the propagating cracks. Their results were found to be

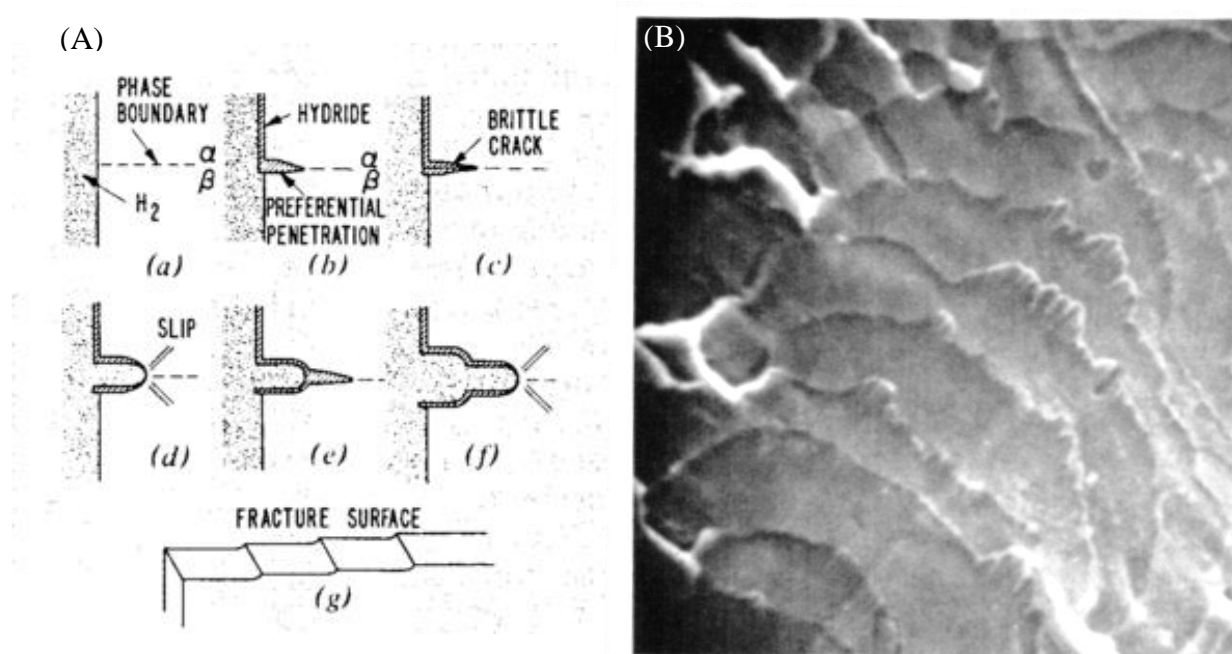


Figure 1.1. (A) Schematic demonstrating film-rupture theory in which hydride formation propagates along alpha-beta interface (b) until it reaches a critical size and crack (c) leading to ductile crack propagation (d) and a repeat of the process (e-f) leading to a fracture surface (g). (B) Fracture surface showing terrace steps of alpha-beta titanium resulting from the presence of gaseous hydrogen.[2]

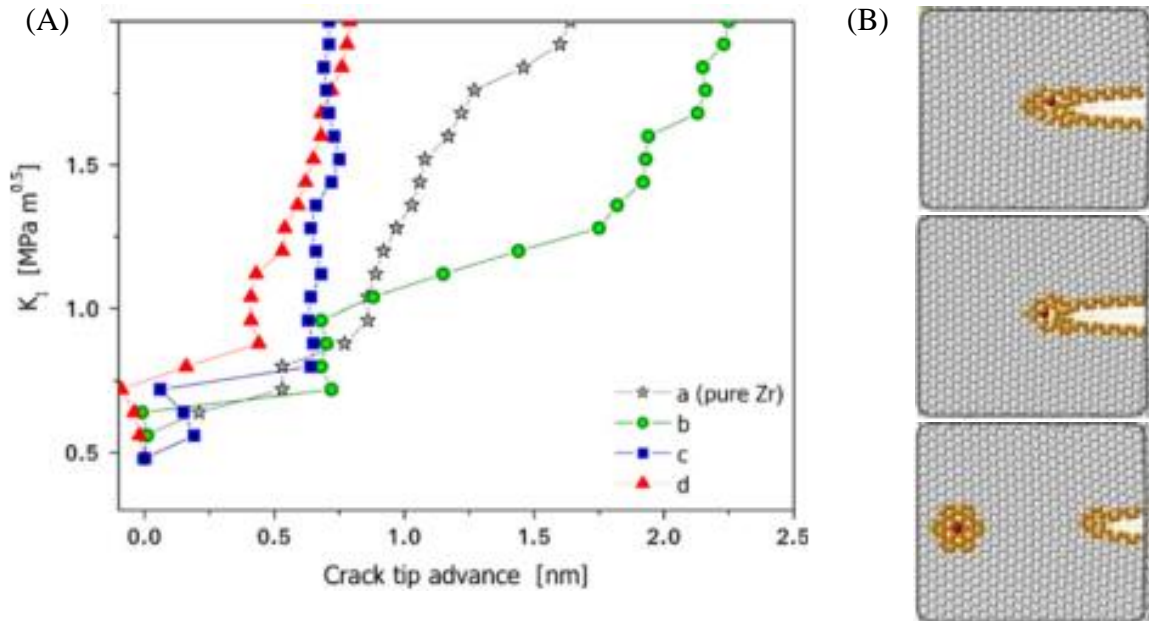


Figure 1.2. (A) Effect of H position ahead of crack tip on stress intensity factor. (B) Initial H (red atom) positions b (top), c (middle), d (bottom).[3]

independent of specimen size and configuration, applied stress intensity magnitude, hydrogen pressure, and the range of temperatures studied.

Computational studies have been performed to explore various aspects of the interactions between hydrogen and zirconium and its alloys. A molecular dynamics study performed by Ruda et al. [3] explored the role of a single H atom on plasticity mechanisms in Zr during crack propagation. Although a single H atom is not sufficient to create a hydride phase, elucidating the effect of a single atom on plasticity is integral to the complete understanding of the formation of hydride phases and subsequent failure mechanisms. Their results showed that the initial position of the H atom ahead of the crack tip has a strong influence on whether the crack propagates, a phase transformation occurs, or if plasticity is generated ahead of the crack tip. The effect of the initial H position on the stress intensity factor,  $K_I$ , is shown in Fig. 1.2.



Another computational study performed by Shmakov et al. [12] used an analysis of the tensile stress distribution in a hydride region ahead of a crack in zirconium alloys to develop a method for computing the critical length and thickness of the hydride layer. They validated their method for computing the critical length and thickness of the hydride layer. They validated their computational model with experimental results on a Zr-2.5% Nb alloy. These computational studies demonstrated that although stress-induced hydride formation has long been an established method of hydrogen embrittlement in hydride forming metals, there is still much work to be done to elucidate the fundamental interactions between H and the metal as well as using the experimental and computational results to increase our ability to predict future failure of materials in corrosive environments.

### 1.1.2 Hydrogen-Induced Decohesion (HID)

Hydrogen-induced decohesion, also known as hydrogen-enhanced decohesion (HEDE), was first proposed in the late 1950's and refers to the reduction of the cohesive force and surface

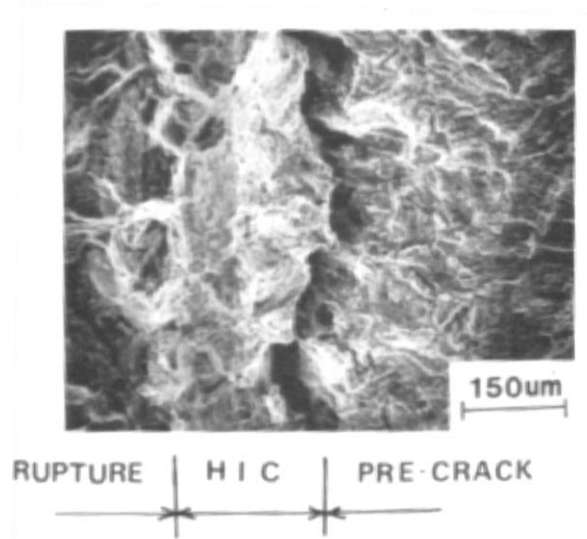


Figure 1.3. Scanning electron micrograph of steel specimen after being loaded in gaseous hydrogen and fractured in air showing the regions and fracture surface structures corresponding to the precrack, the hydrogen induced intergranular cracking, and subsequent rupture [14].

formation energy in the presence of hydrogen [8,9]. Although direct experimental evidence of the HID/HEDE mechanism has yet to be obtained [13], its role in hydrogen embrittlement is supported by observations of failure without significant plastic deformation [14], reduction of fracture strength [15], and by thermodynamic considerations [16–18].

Kameda and McMahon [14] performed four-point bend tests on notched P-, Sn-, and Sb-doped 3.5Ni-1.7Cr steel specimen to study the embrittling effects of gaseous hydrogen under a pressure of 0.17MPa at room temperature and showed that even when small amounts of hydrogen accumulate ahead of a moving crack, the presence of hydrogen led to an increase in intergranular cracking, as shown in Fig. 1.3, when compared to the same doped specimen in air. Figure 1.4 shows that for the doped steel specimen in air, as the doping amount of the respective dopant increases, the values of  $K_{IC}$ , the critical stress intensity parameter, exponentially decreased and similarly, in the presence of hydrogen, as the doping amount of the respective

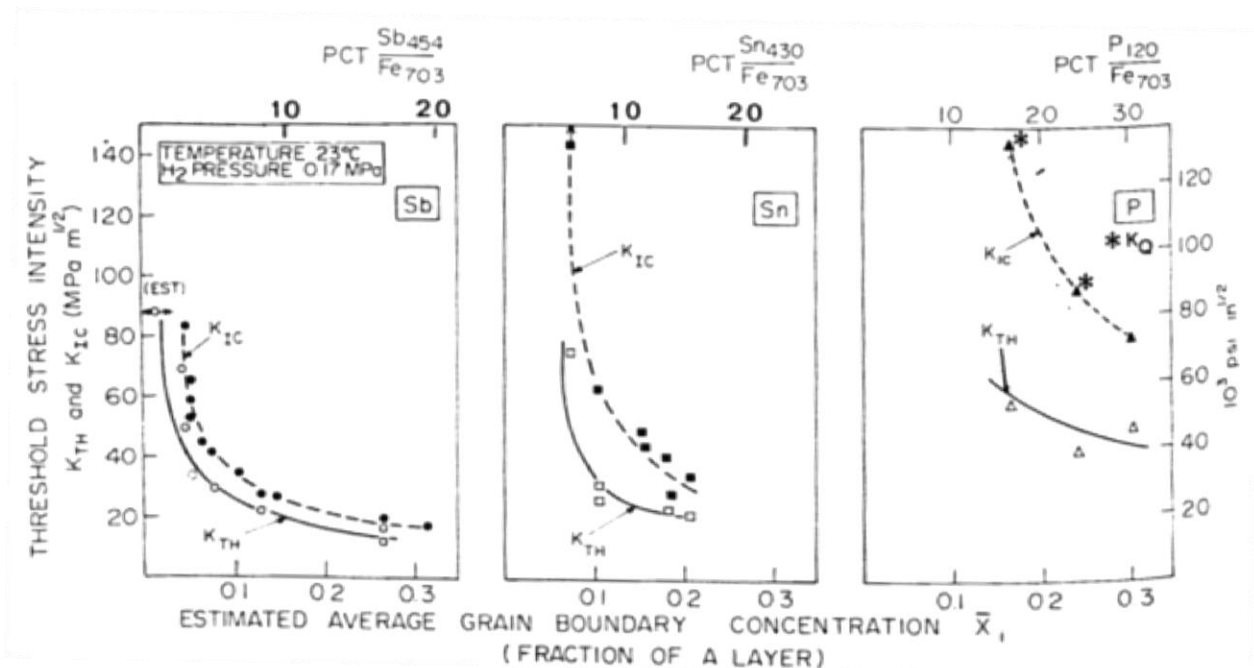


Figure 1.4. Effect of dopant concentrations of Sb, Sn, and P, respectively, on  $K_{IC}$  in air and  $K_{TH}$  in gaseous hydrogen. [14]

dopant increases, the values of  $K_{TH}$ , the threshold stress intensity corresponding to the first detectable crack extension, exponentially decreased. These results imply that the effect of hydrogen diminishes with increasing dopant concentration.

The integral thermodynamic study performed by Hirth and Rice [18] showed that hydrogen directly affects the reversible work of decohesion (ideal work to fracture). This work has been utilized and built upon my many subsequent studies. For example, Mishin et al. [17] numerically studied the presence of impurities on the thermodynamic aspects of interfacial decohesion. Their findings, although not specifically modeling the interactions between hydrogen and a metal, showed that the presence of any impurity serves to decrease the cohesive strength of the interface which can lead to initiation and propagation of a crack in a brittle manner. Their study modeled the decohesion of an interface, in terms of the stresses at the interface, as a function of the diffusion rates or concentrations of the impurities whether they are interstitials or oversized substitutional impurities.

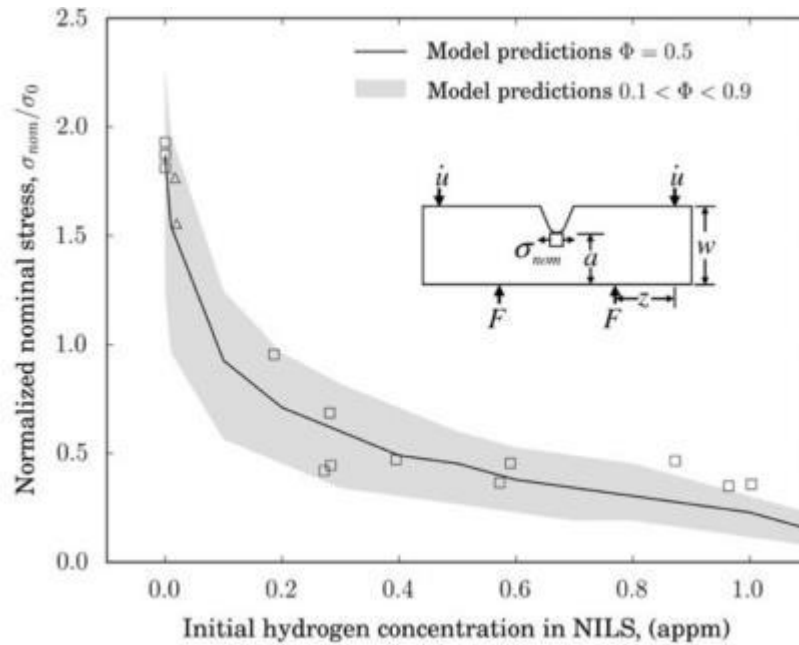


Figure 1.5. Numerically predicted (solid line) and experimental (highlighted area) effect of hydrogen concentration on fracture strength, in terms of normalized nominal bending stress, for single edged-notch type specimen in four point bend test. [5]

Computational studies have also been utilized to potentially explain some of the fundamental mechanisms regarding the reduction in decohesion strength of a material in the presence of hydrogen. Novak et al. [5] used the fundamental results from Hirth and Rice as a foundation to perform finite element simulations to model the degradation in fracture strength of a high-strength steel with various concentrations of hydrogen and were able to verify their results with experiments, as shown in Fig. 1.5. Additionally, ab initio methods have been used to study energetic aspects of the interaction between H and defects in metallic materials including the reduction in cohesive energy in the presence of H in Ni [19], Al and Fe [20], while atomistic simulations have been performed on larger scales to show that H lowered the stress intensity parameter and surface formation energy during crack propagation in Ni [21].

### 1.1.3 Hydrogen-Enhanced Localized Plasticity (HELP)

The HELP mechanism is generally described as an increase in plasticity in a localized region ahead of a crack tip [6] resulting from an increase in dislocation nucleation and mobility and has been extensively studied [22–24]. Experimentally, HELP is motivated by observations of localized ductile crack propagation rather than cleavage fracture ahead of a propagating crack tip [25] and it was shown through high resolution fractography of hydrogenated nickel that there is significant plasticity and dislocation generation localized ahead of the fracture surfaces [23]. Experimental results by Matsumoto et al. [23] showed direct observation, through high voltage electron microscopy (HVEM), of dislocation formation in Ni in the presence of gaseous hydrogen as seen in Fig. 1.6. Similarly, Li et al. [26] showed hydrogen-enhanced dislocation emission and motion in a Ni specimen in the presence of hydrogen relative to the specimen in air, as shown in Fig. 1.7.

Atomistic simulations have been used to explore the fundamental mechanisms resulting in the increase in plasticity ahead of a propagating crack tip. Both ab initio and molecular dynamics simulations have shown that hydrogen leads to the reduction in stacking fault energy in Zr [3,27] which enables enhanced plasticity. Molecular dynamics simulations have also shown that low concentrations of hydrogen at crack tips facilitate dislocation emission [26,28].

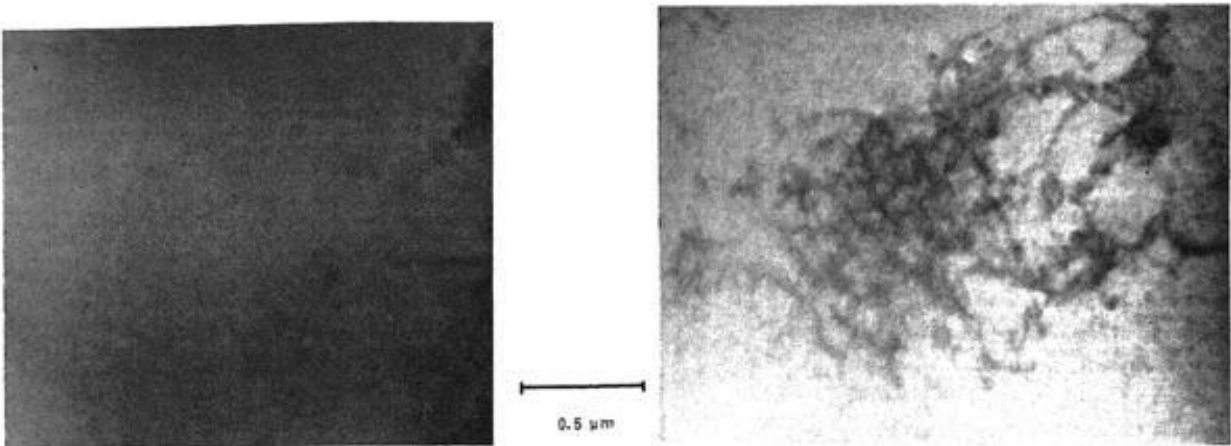


Figure 1.6 HVEM images of strained Ni specimen in vacuum (left) and the same strained region in the presence of gaseous hydrogen at a pressure of 7kPa. [23]

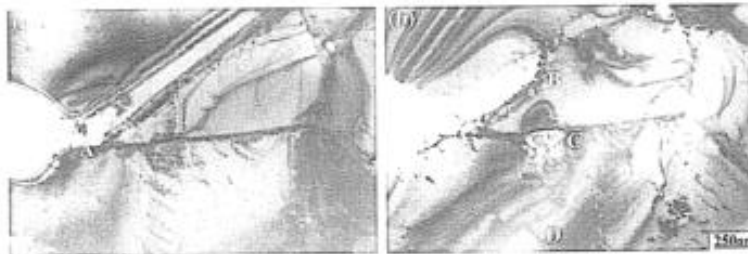


Figure 1.7. TEM images of loaded Ni specimen with crack in air (left) and in gaseous hydrogen (right). Right image taken after 30 minutes of exposure to hydrogen and clearly shows the change in dislocation behavior. [26]

#### 1.1.4 Theory of Coexistent HID and HELP

Although both mechanisms have been extensively studied, a consensus as yet to be reached on whether hydrogen-enhanced localized plasticity or hydrogen-induced decohesion is the

governing mechanism for hydrogen's role in the embrittlement process, or to what extent both mechanisms contribute simultaneously to embrittlement. It is likely that no single mechanism conclusively accounts for premature failure due to hydrogen embrittlement and that the interplay of these mechanisms will further depend on microstructural factors, such as the local structure of the grain boundary or the lattice region ahead of the crack tip.

Gerberich et al. [29] have summarized the interplaying roles of the competing hydrogen-induced decohesion and hydrogen-enhanced localized plasticity mechanisms. They proposed that localized plasticity is always enhanced as dislocation nucleation and velocities of metals are directly affected by the presence of hydrogen, and at crack tips the increased plasticity can lead to dislocation shielding which could promote increased decohesion. In effect, the localized plasticity is a precursor to enhanced decohesion and cleavage. Atomistic simulations seem to support the coexistence of enhanced localized plasticity and enhanced decohesion. Xu et al. [1] explored the effect of H concentration and location on the fracture mechanisms of single crystal Ni under tension and found that low H content facilitated crack propagation and created localized plasticity around the propagating crack tip. Their results showed that in a notched specimen of Ni, increasing the volume fraction of hydrogen atoms localized ahead of the notch leads to a faster reduction in area of the remaining ligament and eventual separation, as shown in Fig. 1. 8, reinforcing the theory of hydrogen-induced decohesion. Additional observations, not shown here, found that low hydrogen content caused the formation of a localized plastic region surrounding the hydrogen at the crack tip, supporting the theory of hydrogen-enhanced localized plasticity.

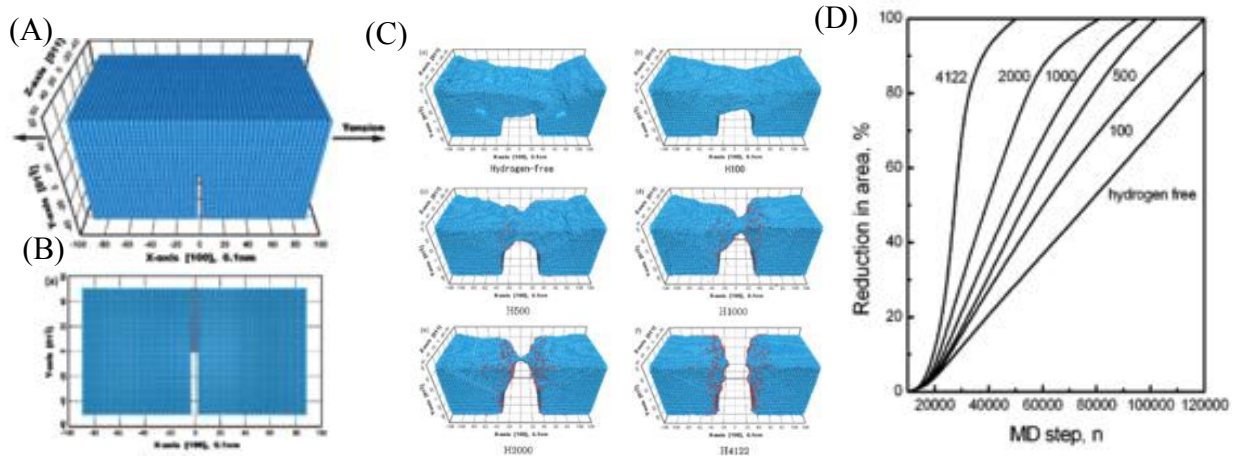


Figure 1.8. (A) Ni notch specimen (B) localized area of hydrogen atom placement (C) simulations at 80,000ps containing (top left) 0, (top right) 100, (mid left) 500, (mid right) 1000, (bottom left) 2000, and (bottom right) 4122 hydrogen atoms (D) reduction in area % with respect to time for different amounts of hydrogen. [1]

## 1.2 Traction-Separation Relationships

The ability to predict the failure of a specimen based on material, geometry, and working conditions is a relatively new development, and thus there are still many areas of fracture mechanics that remain underexplored or not well understood. A basic understanding of the factors governing the generation and propagation of a crack have made it possible to develop numerical modeling software packages that use the finite element method to predict the stress and strain states of modeled specimen. This development has made it possible to provide predictions of failure for virtually any system geometry. A major limitation of these finite element analysis packages is the inability to take into account microstructural or nanostructural considerations, such as grain boundary structure, that are known to affect the fracture mechanics of a material. Independently, atomistic simulations have been developed that can model the failure of a specimen while taking into account the nanostructural orientations, defects, and other various impurities. However, atomistic simulations are severely limited in the time and length

scales that can be simulated due to computational capabilities and resources. Thus arises the need to be able to generate communicable data from atomistic simulations that can be used in larger scale simulations, say finite element method simulations, to more accurately model the failure of a material based on nanostructural considerations rather than solely on bulk material responses and properties.

### 1.2.1 Classical Needleman Type Formulations

In order to relate atomistic interfacial separation to macroscopic separation, Needleman [30] presented a phenomenological methodology which links the normal stress, in the form of a traction vector  $\mathbf{T}$ , to the crack tip opening displacement, referred to as the displacement jump across the interface,  $\Delta$ , through an interface separation potential,  $\phi$ , via the following relationship:

$$\mathbf{T} = -\frac{\partial\phi}{\partial\Delta} \quad \text{Equation 1.1}$$

The development of the interfacial separation potential to model the tractions or stresses as a function of the interfacial separation is based on the cohesive zone interface model [31,32]. The interface separation potential is intended to characterize fracture behavior (decohesion strength and work of separation) and is posed as a differentiable analytic expression. A wide variety of analytic forms have been proposed including a second degree polynomial [30], as shown in Fig. 1.9, and various exponential functions [33–35]. The form of the interfacial separation potential has been shown [34] to have a large effect on the results of finite element simulations. Together, Needleman type interfacial separation potentials and macroscale finite element methods have been used to model interfacial void nucleation to total interfacial decohesion. These, and other



continuum separation potentials, however, do not take into explicitly account the atomistic scale interactions taking place during crack nucleation and propagation.

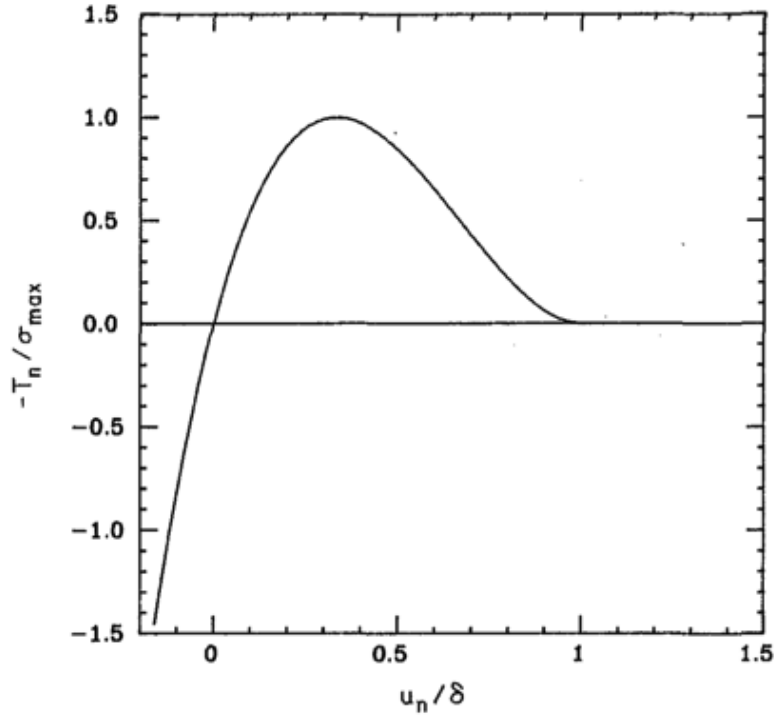


Figure 1.9: Example of normal traction,  $T_n$ , as a function of the normalized opening displacement,  $u_n$ , where the traction and opening displacement have been normalized by the cohesive strength,  $\sigma_{\max}$ , and a characteristic length,  $\delta$ , respectively. [34]

### 1.2.2 Efforts to Derive Traction-Separation Relationships from Atomistic Simulations

An increasing amount of focus has been put into generating constitutive relationships that mirror or more accurately model interfacial separation in ductile materials where energy dissipative mechanisms are prevalent during crack nucleation and propagation. Recent studies have sought to develop methodologies to extract traction-separation relationships from molecular dynamics simulations using an atomistic model analogous to the cohesive zone interface model [36–41]. Although these models represent promising improvements on previous works, they do not attempt to differentiate the decohesion response of the interface from the intrinsic elastic

properties, such as the elastic stiffness of the interface. A primary goal of this thesis is to improve upon the some aspects of the work of Yamakov et al. [37] by improving the understanding of the interplay between the decohesion and elastic stiffness responses of the interface in the extraction of the traction-separation relationship for a ductile material.

### 1.3 Thesis Objectives and Structure

There are three main objectives to this thesis: (i) to develop a numerical methodology to extract traction-separation relationships from data obtained through atomistic simulations; (ii) to apply the numerical methodology to specific grain boundary systems with different amounts of hydrogen located at the grain boundary interface; (iii) to further the understanding, based on the traction-separation relationships, of the mechanisms by which hydrogen effects the decohesion of a grain boundary system.

Chapter 2 provides a basic overview of the theory of atomistic simulations with particular focus on atomistic simulation methods used in this work. First, the concept of an interatomic potential is introduced. The interatomic potential provides a model for the potential energy of an ensemble of atoms based on their relative positions and allows for the derivation of the forces between atoms, a concept without which atomistic simulations would not be possible. Next, Monte Carlo simulations are briefly introduced as a method for determining minimum energy configurations of a group of atoms. In this work, Monte Carlo simulations are performed by collaborators at Sandia National Laboratories to determine the most energetically favorable sites for hydrogen atoms within bicrystal Ni grain boundaries. This is done for three grain boundary systems, discussed in Chapters 3 and 4, where the amount of hydrogen included in the system is based on the chemical potential [42]. Then, two types of classical mechanics based simulations,

Molecular Statics and Molecular Dynamics, are discussed. Throughout this work, molecular statics simulations are performed to determine the minimum energy configuration of a set of atoms. More specifically, they are used to determine the minimum energy grain boundary configurations or interface structures in the absence of temperature, and to ensure that hydrogen atoms occupy the most energetically favorable positions at or within the grain boundary. These are important steps as they ensure that the interface structures and hydrogen locations are consistent with previous work and experiment allowing for quantitative comparison. Lastly, molecular dynamics simulations are discussed extensively. Specifically the NPT ensemble is used to equilibrate the system of atoms under a hydrostatic stress. This stress stretches the atomic bonds in three dimensions and provides a driving force for propagation of the crack that is introduced within the grain boundary during the subsequent NVT equilibration.

Chapter 3 details the methodology to extract the traction-separation relationship from atomistic simulations. Briefly, atomistic simulations are performed in LAMMPS [43] which generates output data containing the stress and positions of the atoms. By dividing the region surrounding the grain boundary interface into rectangular volume elements, called Cohesive Zone Volume Elements (CZVEs), the average center of mass position and tensile stress are determined for each CZVE. The averaging serves to eliminate simulation effects such as phonon wave propagation during crack propagation and thermal vibrations due to temperature. The traction-separation relationship is extracted by fitting a curve to the average CZVE data when plotted as traction, or average stress, versus the separation between neighboring CZVE pairs across the grain boundary interface. In Chapter 3, six Ni  $\Sigma 3(112)[1\bar{1}0]$  grain boundary systems are analyzed using the methodology, where the six systems differ in the amount of atomic hydrogen that has been added to energetically favorable positions within the grain boundary

interface. The amount of hydrogen added to the grain boundary interface is relative to the maximum number of hydrogen atoms that could populate the grain boundary interface based on the favorable hydrogen atom locations determined via Monte Carlo simulations [42]. Hydrogen atoms are added to give hydrogen atoms occupying 0%, 25%, 50%, 66.4%, 75%, and 100% of the energetically favorable positions, where 0% represents a pure Ni system with no H atoms, 66.4% represents a system with the equilibrium concentration of H atoms as governed by the chemical potential, and 100% represents the case where every favorable position within the grain boundary has been populated by a H atom. Two traction-separation curves are generated for each of the six systems, one for propagation of the center-crack in the positive direction (right) and one for propagation in the negative direction (left).

Chapter 4 details the application of the numerical methodology outlined Chapter 3 to extract traction-separation relationships from two grain boundaries that have misorientations near the symmetric tilt coherent twin  $\Sigma 3(111)[1\bar{1}0]$  grain boundary. These two misoriented twin grain boundaries have orientations with rotations about the misorientation axis both greater than (interior:  $+8.89^\circ$ ) and less than (exterior:  $-10.10^\circ$ ) the rotation of the  $109.5^\circ$  misorientation associated with the coherent twin grain boundary. The purpose of simulating these near coherent is to demonstrate the robustness of the developed methodology to extract the traction-separation curves and associated properties from virtually any grain boundary system with or without the inclusion of atomic hydrogen segregated to the grain boundary.

#### 1.4 References

- [1] Xu X, Wen M, Fukuyama S and Yokogawa K 2001 Simulation of hydrogen embrittlement at crack tip in nickel single crystal by embedded atom method *Mater. Trans.* **42** 2283–9

- [2] Nelson H G 1976 A Film-Rupture Model of Hydrogen-Induced, Slow Crack Growth in Acicular Alpha-Beta Titanium *Metall. Trans. Phys. Metall. Mater. Sci.* **7** 621–7
- [3] Ruda M, Bertolino G, Farkas D and Baruj a. 2013 Effect of dilute H on crack tip plasticity in Zr *Comput. Mater. Sci.* **69** 327–34
- [4] Birnbaum H K and Sofronis P 1994 Hydrogen-enhanced localized plasticity--a mechanism for hydrogen- related fracture *Mater. Sci. Eng. A* **176** 191–202
- [5] Novak P, Yuan R, Somerday B P, Sofronis P and Ritchie R O 2010 A statistical, physical-based, micro-mechanical model of hydrogen-induced intergranular fracture in steel *J. Mech. Phys. Solids* **58** 206–26
- [6] Beachem C D 1972 New model for hydrogen- assisted cracking (hydrogen “embrittlement”) *Metall. Trans.* **3** 437–51
- [7] Troiano A R 1960 Embrittlement by Hydrogen and Other Interstitials *Met. Prog.* **77** 112–7
- [8] Steigerwald E A, Schaller F W and Troiano A R 1960 Role of stress in hydrogen induced delayed failure *Metall. Soc. Am. Inst. Mining, Metall. Pet. Eng. -- Trans.* **218** 832–41
- [9] Oriani R A and Josephic P H 1974 Equilibrium aspects of hydrogen-induced cracking of steels *Acta Metall.* **22** 1065–74
- [10] Hardie D and McIntyre P 1973 The low-temperature embrittlement of niobium and vanadium by both dissolved and precipitated hydrogen *Metall. Trans.* **4** 1247–54
- [11] Gahr S, Grossbeck M L and Birnbaum H K 1977 Hydrogen embrittlement of Nb I— Macroscopic behavior at low temperatures *Acta Metall.* **25** 125–34
- [12] Shmakov a, Yan D and Eadie R 2006 A theoretical and experimental study of hydrides in zirconium alloys *Met. Sci. Heat Treat.* **48** 146–9
- [13] Sofronis P and Robertson I M 2006 Viable mechanisms of hydrogen embrittlement - A review *AIP Conf. Proc.* **837** 64–70
- [14] Kameda J and McMahon Jr. C J 1983 Solute Segregation and Hydrogen-Induced Intergranular Fracture in an Alloy Steel *Metall. Trans. Phys. Metall. Mater. Sci.* **14 A** 903–11
- [15] Dadfarnia M, Somerday B P, Schembri P E, Sofronis P, Foulk J W, Nibur K a. and Balch D K 2014 On Modeling Hydrogen-Induced Crack Propagation Under Sustained Load *Jom* **66**

- [16] Hirth J P 1980 Effects of Hydrogen on the Properties of Iron and Steel *Metall. Trans. Phys. Metall. Mater. Sci.* **11** 861–90
- [17] Mishin Y, Sofronis P and Bassani J L 2002 Thermodynamic and kinetic aspects of interfacial decohesion *Acta Mater.* **50** 3609–22
- [18] Hirth J P and Rice J R 1980 On the thermodynamics of adsorption at interfaces as it influences decohesion *Metall. Trans. A* **11** 1501–11
- [19] Geng W, Freeman a., Wu R, Geller C and Reynolds J 1999 Embrittling and strengthening effects of hydrogen, boron, and phosphorus on a  $\Sigma 5$  nickel grain boundary *Phys. Rev. B* **60** 7149–55
- [20] Jiang D E and Carter E a. 2004 First principles assessment of ideal fracture energies of materials with mobile impurities: Implications for hydrogen embrittlement of metals *Acta Mater.* **52** 4801–7
- [21] Solanki K N, Ward D K and Bammann D J 2011 A nanoscale study of dislocation nucleation at the crack tip in the nickel-hydrogen system *Metall. Mater. Trans. A Phys. Metall. Mater. Sci.* **42** 340–7
- [22] Teter D F, Robertson I M and Birnbaum H K 2001 The effects of hydrogen on the deformation and fracture of  $\alpha$ -titanium *Acta Mater.* **49** 4313–23
- [23] Matsumoto T, Eastman J and Birnbaum H K 1981 Direct observations of enhanced dislocation mobility due to hydrogen *Scr. Metall.* **15** 1033–7
- [24] Lynch S P 1988 Environmentally assisted cracking: Overview of evidence for an adsorption-induced localised-slip process *Acta Metall.* **36** 2639–61
- [25] Eastman J, Matsumoto T, Narita N, Heubaum F and Birnbaum H K 1981 Hydrogen Effects in Nickel - Embrittlement or Enhanced Ductility? *Hydrogen Effects in Metals: Proceedings of the 3rd International Conference on Effect of Hydrogen on Behavior of Materials.* (Moran, WY, USA: Metall Soc of AIME) pp 397–409
- [26] Li Z, Li J, Chu W, Liu H and Qiao L 2002 Molecular dynamics simulation and experimental proof of hydrogen-enhanced dislocation emission in nickel *J. Univ. Sci. Technol. Beijing Miner. Metall. Mater. (Eng Ed)* **9** 59–64
- [27] Domain C, Besson R and Legris B 2004 Atomic-scale ab initio study of the Zr-H system: II. Interaction of H with plane defects and mechanical properties *Acta Mater.* **52** 1495–502
- [28] Daw M S, Baskes M I, Bisson C L and Wolfer W G 1986 Application of the Embedded Atom Method to Fracture, Dislocation Dynamics, and Hydrogen Embrittlement. *Modeling Environmental Effects on Crack Growth Processes. Proceedings of a Symposium Held at*

- the 1985 Fall Meeting of the Metallurgical Society.* (Sandia Natl Lab, Livermore, CA, USA, Sandia Natl Lab, Livermore, CA, USA: Metallurgical Soc of AIME) pp 99–124
- [29] Gerberich W W and Stauffer D D 2009 A Coexistent View of Hydrogen Effects on Mechanical Behavior of Crystals: HELP and HEDE *Effects of hydrogen on materials, ASM International, Materials Park, OH* pp 38–45
- [30] Needleman a. 1987 A Continuum Model for Void Nucleation by Inclusion Debonding *J. Appl. Mech.* **54** 525
- [31] Dugdale D S 1960 Yielding of Steel Sheets Containing Slits *J. Mech. Phys. Solids* **8** 100–4
- [32] Barenblatt G I 1959 Concerning equilibrium cracks forming during brittle fracture. The stability of isolated cracks. Relationships with energetic theories *J. Appl. Math. Mech.* **23** 1273–82
- [33] Needleman a. 1992 Micromechanical modelling of interfacial decohesion *Ultramicroscopy* **40** 203–14
- [34] Needleman A 1990 An analysis of tensile decohesion along an interface *J. Mech. Phys. Solids* **38** 289–324
- [35] Xu X P and Needleman A 1993 Continuum Modelling of Interfacial Decohesion *Solid State Phenom.* **35-36** 287–302
- [36] Yamakov V, Saether E, Phillips D R and Glaessgen E H 2005 Dynamic instability in intergranular fracture *Phys. Rev. Lett.* **95** 1–4
- [37] Yamakov V, Saether E and Glaessgen E H 2008 Multiscale modeling of intergranular fracture in aluminum: Constitutive relation for interface debonding *J. Mater. Sci.* **43** 7488–94
- [38] Yamakov V, Saether E, Phillips D R and Glaessgen E H 2006 Molecular-dynamics simulation-based cohesive zone representation of intergranular fracture processes in aluminum *J. Mech. Phys. Solids* **54** 1899–928
- [39] Li Y-L, Wu W-P, Li N-L and Qi Y 2015 Cohesive zone representation of crack and void growth in single crystal nickel via molecular dynamics simulation *Comput. Mater. Sci.* **104** 212–8
- [40] Zhou X W, Zimmerman J a., Reedy E D and Moody N R 2008 Molecular dynamics simulation based cohesive surface representation of mixed mode fracture *Mech. Mater.* **40** 832–45

- [41] Spearot D E, Jacob K I and McDowell D L 2004 Non-local separation constitutive laws for interfaces and their relation to nanoscale simulations *Mech. Mater.* **36** 825–47
- [42] O’Brien C J and Foiles S M 2014 *Private Communication*
- [43] Plimpton S 1995 Fast Parallel Algorithms for Short-Range Molecular-Dynamics *J. Comput. Phys.* **117** 1–19



## CHAPTER 2: BACKGROUND

### 2.1 Atomistic Simulations

Atomistic simulation refers to a variety of computational techniques that are employed to predict properties, characteristics, and response of a system of atoms that is often subjected to some internal or external stimulus. Even at the atomic level, a material can be modeled in many different ways; the two primary modeling approaches are based on quantum mechanical or classical mechanical considerations. Quantum mechanical based simulations accurately model atomic arrangements by taking into account both atoms and their associated electrons; however, quantum mechanical simulations can quickly become computationally expensive with the inclusion of more than a few hundred atoms and their corresponding electrons. The types of quantum mechanical simulations differ in how they approximate the solutions to the Schrödinger equation that determines the configuration of the electrons surrounding the nuclei of the atoms. A full discussion of quantum mechanical modeling techniques is beyond the scope of this thesis.

On the other hand, classical mechanics based simulations model atoms as interacting unified spheres with a defined mass, and their trajectories and interactions are determined in accordance with Newton's Laws of Motion and an interatomic potential. The simplification of atomic structure into a unified sphere dramatically reduces the number of degrees of freedom of the system, thus reducing the number of equations that need to be solved to determine the state of the system and increasing the number of atoms that can be simulated to the tens of millions, or even billions on the World's largest computers [44,45]. However, because the electrons and their role in structure and energy determination are ignored, there arises a need for an alternative method for determining the potential energy, and thus the force, between a pair of atoms. The interatomic

potential is a mathematical function that defines the potential energy,  $U$ , of a system of atoms based on their relative positions,  $\mathbf{r}$ , to each other. Because the interatomic forces are conserved in a system, the force on any atom,  $\mathbf{F}^i$ , can be determined from the interatomic potential. The interatomic potential along with the specific interatomic potential for Ni-H used in this work will be discussed in more detail in Section 2.2. There are three primary types of classical mechanics based atomistic simulations: Monte Carlo, molecular statics, and molecular dynamics; all of which are used in this work and will be discussed in Section 2.3, Section 2.4, and Section 2.5, respectively.

Although classical atomistic simulations have the capability of simulating systems with up to tens of millions of atoms, this still does not come close to simulating macroscale systems which have on the order of  $10^{23}$  atoms. Various efforts have been made to minimize the effects of only simulating a finite size block of atoms, the most relevant to this work, is the implementation of periodic boundary conditions. The primary benefit of periodic boundary conditions is that they eliminate the free surfaces that are created at the boundaries of the simulation system, which can greatly influence the behavior of the material. Illustrated in Fig. 2.1, a two-dimensional simulation cell containing atoms explicitly modeled using classical atomistic simulation methods, highlighted in yellow, is surrounded by bordering ‘image’ cells, which are not highlighted [46]. Atoms in these ‘image’ cells are not explicitly modeled, but can be seen as ‘copied’ atoms across the periodic boundary of the explicitly modeled primary cell. Atoms located near the bounds of the explicitly modeled primary cell may move during the course of a simulation, and may pass across the boundaries of the cell. Rather than being reflected, the atom is able to pass through the boundary and into one of the ‘image’ cells while an atom with the same properties in the opposite ‘image’ cell simultaneously passes through the opposite

boundary and into the primary cell. This is illustrated with the red trajectory arrow of the gray highlighted atom in Fig. 2.1. Thus, periodic boundary conditions, in effect, create an infinite material devoid of unnecessary free surfaces arising as artifacts of the simulated system's finite size.

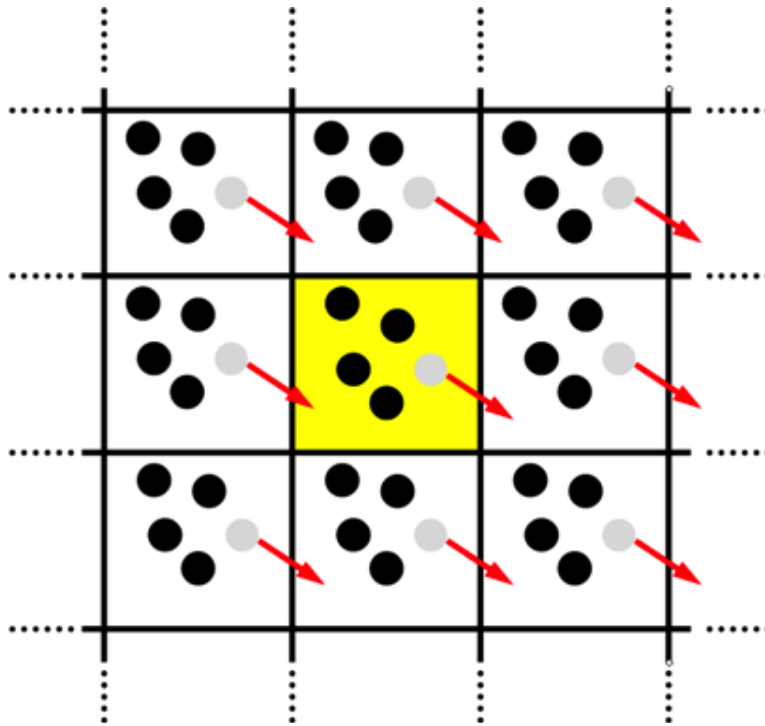


Figure 2.1. Two-dimensional illustration of periodic boundary conditions. [46]

Particular attention must be paid to the size of the simulated cell, taking into account both the cutoff distance defined in the interatomic potential, and long range effects associated with the type of simulation being performed. For this work, the cutoff distance defined by the interatomic potential is dwarfed by the long range effects associated with crack propagation and decohesion, thus, rather large systems are simulated. During crack propagation, a crack or void is replicated in the infinite 'image' cells, creating cracks or voids that could possibly 'feel' each other resulting in physically impossible self-interactions. In order to reduce the effects of this 'self-interaction' the system must be necessarily large.

## 2.2 Interatomic Potential

### 2.2.1 Introduction

As mentioned in Section 2.1 an interatomic potential is a mathematical function that is used to determine the potential energy,  $U$ , between two or more atoms in a system based on their proximity or relative positions,  $\mathbf{r}$ , while ignoring the electrons and their role in structure and energy determination. Usually, the total potential energy of the system,  $U_{sys}$ , is computed by adding up the pairwise potential energies for every pair of atoms in the system, where two atoms are considered a pair if their proximity,  $\mathbf{r}$ , is less than some defined cutoff distance,  $\mathbf{r}_{cutoff}$ . The implementation of  $\mathbf{r}_{cutoff}$  ensures that only atoms sufficiently close to another atom to have a non-negligible potential energy or interaction force are accounted for, thus eliminating unwarranted computations. The interatomic forces acting on any atom,  $\mathbf{F}_i$ , can be determined by taking the gradient,  $\partial / \partial \mathbf{r}$ , of the sum of potential energies of that atom, taking into account the fact that there are no dissipative forces acting on the system of atoms and thus that all forces are conserved, via the following relationship:

$$\mathbf{F}_i = - \frac{\partial U_{sys}}{\partial \mathbf{r}_i} \quad \text{Equation 2.1}$$

There are many types of interatomic potentials that range in complexity from the simple pair-potential, which only accounts for energy effects based on local proximity, to many-body cluster potentials, which account for energies associated with the distance and local arrangement of three or four atoms. Another type of interatomic pair-potential is the embedded-atom method (EAM) interatomic potential, which accounts for the energies associated with both interactions between pairs of atoms and local electron densities computed from the positions of the atoms

surrounding the pair. In effect, it models the energy required to embed an atom as an impurity into a lattice of other atoms while taking into account the electron density at the embedding point. The EAM potential has been used to model many metallic systems [47].

## 2.2.2 Ni-H Interatomic Potential

All simulations in this work are performed using an embedded-atom method (EAM) interatomic potential for Ni-H that models the effects on the potential energy of both nickel and hydrogen atoms from surrounding nickel and hydrogen atoms [47]. This EAM potential has been shown to accurately predict many properties that are of particular influence to this work, such as: bulk cohesive energy, elastic constants, the intrinsic stacking fault energy, and vacancy formation energy in Ni [47], as shown in Table 2.1.

Parameter	Fit	Experimental
$a_0$	[3.52]	3.52 [35]
$E_{Coh}$	[4.45]	4.45 [36]
* $C_{11}$	2.464	2.465 [37]
* $C_{12}$	1.473	1.473 [37]
* $C_{44}$	1.248	1.247 [37]
* $E_f^v$	1.59	1.6 [38]
* $E^{sf}$	89	125 [39]
* $E_{BCC} - E_{FCC}$	0.06	0.06 [40]
$E_{100}^s$	2060	2380 <sup>a</sup> [41]
$E_{110}^s$	2350	
$E_{111}^s$	1928	
$v_{100}^l$	9.86	8.55 [42]
$v_{100}^t$	6.44	6.27 [42]

<sup>a</sup> Average face value.

Table 2.1. Quantities that are fitted (distinguished by \* or, if guaranteed to be correct by square brackets, []) and predicted by the embedded atom method. The vacancy formation energy,  $E_f^v$ , and cohesive energy,  $E_{Coh}$ , are both in eV, the stacking fault energy,  $E^{sf}$  is in  $\text{erg}\cdot\text{cm}^{-2}$ , and the elastic constants,  $E_{1**}^s$ , are in  $10^{12} \text{ dyn}\cdot\text{cm}^{-2}$ . [47]

## 2.3 Monte Carlo Simulations

In this work, Monte Carlo simulations are performed to determine the most energetically favorable positions within the grain boundary structure for hydrogen atoms to occupy. Monte Carlo simulations are purely stochastic simulation methods that use random numbers to sample different configurations of atoms in order to randomly explore all possible atomistic configurations. In atomistic Monte Carlo simulations, the Metropolis method [48] is most often used to determine the lowest energy configurations of a system of atoms. These simulations are often performed on systems with a fixed number of atoms or molecules,  $N$ , that occupy a fixed volume,  $V$ , with a constant absolute temperature,  $T$  [49,50].

To determine the minimum energy configuration of a system of  $N$  atoms with initial positions,  $\mathbf{r}_i$ , and with a resulting initial potential energy,  $U$ , one of the  $N$  atoms is randomly chosen and displaced by a random vector,  $\delta\mathbf{r}$ , which is usually bounded by a maximum magnitude,  $\delta\mathbf{r}_{max}$ . Based on the potential energy of the system with the displaced atom,  $U'$ , the new configuration (i) can be accepted in which case the displacement of the atom is allowed and the resulting configuration becomes the initial configuration for a subsequent random selection and displacement, (ii) can be rejected in which case the move is denied and the initial configuration remains and the process continues. If the potential energy of the resulting system is lower than the initial potential energy, i.e.  $U' < U$ , the move is always accepted. If the potential energy of the resulting system is higher than the initial potential energy, i.e.  $U' \geq U$ , the move can be accepted with a probability of  $\exp(-\beta\Delta U)$ , where  $\beta = 1/kT$ ,  $k$  is Boltzmann's constant, and  $\Delta U = U' - U$ . The merit of accepting seemingly unfavorable moves is to increase the number of sampled configurations in determining the overall minimum energy configuration.

## 2.4 Molecular Statics Simulations

In this work, molecular statics simulations are performed to generate grain boundaries with minimum energy, or most favorable, interface structures that are consistent with prior studies, thus ensuring that a reliable comparison can be made between this work and prior research. Molecular statics simulations are a form of classical atomistic simulations that are implemented to determine minimum energy structures in the absence of temperature effects, i.e., they are performed at 0K. Energy minimization is a process by which atoms are allowed to move from their initial positions with increments and directions that result in a decrease in the overall potential energy of the system. The energy minimization approach used in this work utilizes the conjugate gradient minimization method. The conjugate gradient method is a method for solving large systems of linear equations [51] for a set of inputs, atom positions in the case of atomistic simulations, that minimize a desired quantity, the potential energy in the case of atomistic simulations. Ultimately, this is done through an iterative approach with minimum potential energy determined once the difference between the potential energy at one step and the potential energy at the next step is less than a user-defined threshold value. A more detailed explanation of the atomistic conjugate gradient method, and other minimization methods for solving systems of equations, can be found in Shewchuk [51].

## 2.5 Molecular Dynamics Simulations

In this work, molecular dynamics (MD) simulations are performed to investigate the fundamental mechanisms by which a crack propagates along a grain boundary interface in the presence of atomic hydrogen. As mentioned in Section 2.1, molecular dynamics simulations are a type classical atomistic simulation where atoms are modeled as unified spheres whose motions

are governed by classical mechanics equations, that is Newton's 2<sup>nd</sup> Law of motion (or augmented versions of Newton's 2<sup>nd</sup> Law when control of temperature and pressure is desired),

$$\dot{\mathbf{p}}^i = \mathbf{F}^i = m \frac{d\mathbf{r}^i}{dt} = m\mathbf{v}^i \quad \text{Equation 2.2}$$

where  $\mathbf{p}^i$  is the momentum vector of the  $i^{\text{th}}$  atom,  $\mathbf{F}^i$  is the net force vector on the  $i^{\text{th}}$  atom,  $m$  is the mass of the atom,  $\mathbf{r}^i$  is the position of the  $i^{\text{th}}$  atom, and  $\mathbf{v}^i$  is the velocity of the  $i^{\text{th}}$  atom.

Equation 2.2 serves as the foundation of molecular dynamics simulations.

Performing a molecular dynamics simulation requires three basic steps that must be performed. First, a system of atoms must be created and assigned initial positions or velocities if necessary. The initialization of the system is discussed in Section 2.4.1. Next, the thermodynamic state of the system must be fixed. Fixing the thermodynamic state of the system defines the equations of motion that the trajectories of the atoms will follow. The different types of fixes that define the thermodynamic state of the system are discussed in Section 2.4.2. Finally, the equations of motion that are defined by fixing the thermodynamic state of the system must be solved or integrated every timestep to update the positions and velocities of the atoms. The velocity-Verlet method for solving the coupled differential equations is described in Section 2.4.3.

### 2.5.1 Initializing the System

The first step in performing a molecular dynamics simulation on a system is to create the initial system. This initialization requires the definition of the number of atoms, their positions, and velocities if necessary. With a set number of atoms, in LAMMPS [43] it is common to define the initial positions of the atoms via a lattice, e.g., a face-centered cubic (FCC) lattice with a lattice



parameter of 3.52Å for Ni. If the system is to be created with an initial temperature, the velocities of the N atoms are assigned randomly within a Gaussian distribution with the constraints that the net or sum of the velocities must be 0, as the system is stationary, and the average velocity is consistent with the defined temperature. The second constraint is imposed by scaling the atom velocities based on the temperature using Equation 2.3 where  $k_B$  is Boltzmann's constant [50]:

$$T(t) = \frac{1}{3k_B N} \sum_{i=1}^N m_i v_i^2 \quad \text{Equation 2.3}$$

### 2.5.2 Thermodynamic State of the System

There are three notable molecular dynamics ensembles that differ in how the coupled equations of motion are solved and whether additional equations are necessary to model various effects from the outside environment on the otherwise isolated system of atoms, the microcanonical (NVE), the isothermal-isobaric (NPT), and the canonical (NVT) ensembles. These ensembles effectively fix the thermodynamic state of the system. The microcanonical ensemble is used to simulate isolated systems with a fixed number of atoms, N, occupying a fixed volume, V, with a fixed internal energy, E, and whose atom trajectories are governed only by Equation 2.2. The microcanonical ensemble is not used in this work, however the NPT and NVT ensembles are used in this work and are discussed for the remainder of this section. When employing these ensembles, the appropriate properties are allowed to fluctuate around a constant value while time integrations are performed on the equations of motion. The positions and velocities of each atom are updated every timestep, which is defined as 1fs or 1E-15s in this work. The equations of motion associated with the NPT and NVT ensembles that are used in

LAMMPS [43] are those of Shinoda et al. [52] which contain modifications to the Nosé-Hoover equations of motion [53]:

$$\begin{aligned}
\dot{\mathbf{r}}_i &= \frac{\mathbf{p}_i}{m_i} + \frac{\mathbf{p}_g}{W_g} \mathbf{r}_i \\
\dot{\mathbf{p}}_i &= \mathbf{F}_i - \frac{\mathbf{p}_g}{W_g} \mathbf{p}_i - \frac{1}{N_f} \frac{\text{Tr}[\mathbf{p}_g]}{W_g} \mathbf{p}_i - \frac{p_{\xi}}{Q} \mathbf{p}_i \\
\dot{\mathbf{h}} &= \frac{\mathbf{p}_g}{W_g} \mathbf{h} \\
\dot{\mathbf{p}}_g &= V(\mathbf{P}_{int} - \mathbf{I}P_{ext}) - \mathbf{h}\boldsymbol{\Sigma}\mathbf{h}^t + \left( \frac{1}{N_f} \sum_{i=1}^N \frac{\mathbf{p}_i^2}{m_i} \right) \mathbf{I} - \frac{p_{\xi_1}}{Q_1} \mathbf{p}_g \\
\dot{\xi}_k &= \frac{p_{\xi_k}}{Q_k} \text{ for } k = 1, \dots, M \\
\dot{p}_{\xi_1} &= \sum_{i=1}^N \frac{\mathbf{p}_i^2}{m_i} + \frac{1}{W_g} \text{Tr}[\mathbf{p}_g^t \mathbf{p}_g] - (N_f + d^2)kT_{ext} - p_{\xi_1} \frac{p_{\xi_2}}{Q_2} \\
\dot{p}_{\xi_k} &= \left( \frac{p_{\xi_{k-1}}^2}{Q_{k-1}} - kT_{ext} \right) - p_{\xi_k} \frac{p_{\xi_{k+1}}}{Q_{k+1}} \text{ for } k = 2, \dots, M-1 \\
\dot{p}_{\xi_M} &= \left( \frac{p_{\xi_M}^2}{Q_M} - kT_{ext} \right)
\end{aligned} \tag{Equation 2.4}$$

where, taking from Shinoda [52], the variables  $\mathbf{r}_i$  is the position, and  $\mathbf{p}_i$  is the momentum of atom  $i$ ,  $\mathbf{h}$  is the cell matrix,  $\mathbf{p}_g$  is the modularly invariant form of the cell momenta,  $\xi_k$  and  $p_{\xi_k}$  are the thermostat variable and its conjugated momentum of the  $k$ th thermostat, and the constants  $m_i$  is the mass of atom  $i$ ,  $W_g$  is the barostat,  $Q_k$  is the  $k$ th thermostat, and  $N_f$  is the number of degrees of freedom of the system and is equal to  $3N$ . Additionally,  $V$  is the system volume,  $\mathbf{P}_{int}$  is the internal pressure in the system,  $P_{ext}$  is the hydrostatic pressure acting on the system,  $\mathbf{I}$  is the identity matrix,  $T_{ext}$  is the external temperature, and  $\boldsymbol{\Sigma}$  is a matrix that modifies the cell matrix. The equations of motion in Equation 2.4 are for the Nosé-Hoover chain thermostat method, whereas the value of  $M$ , the chain length, is 1 for molecular dynamics simulations. Further information on these equations, the constants and variables, and the properties and

utilization of these equations can be found in Shinoda et al. [52]. Note that the first two equations in Equation 2.4 are simply modified versions of the classical equations of motion in Equation 2.2, and the additional equations are included to ensure that the atoms' velocities and the bounds of the system, which determine the systems volume, are able to change based on the defined pressure and temperature of the system.

### 2.5.3 Velocity Verlet Integration Technique

Whether using the relatively simple equations of motion in Equation 2.2 or the more complex equations of motion in Equation 2.4 [52], the algorithm used for solving these coupled first order ordinary differential equations for an N-body system is the same. For the NVE ensemble (Equation 2.4), the velocity-Verlet algorithm updates the positions and velocities of the atoms via the following:

$$\begin{aligned} \mathbf{r}_i(t + \Delta t) &= \mathbf{r}_i(t) + \Delta t \mathbf{v}_i(t) + \frac{1}{2}(\Delta t)^2 \mathbf{a}_i(t) \\ \mathbf{v}_i(t + \Delta t) &= \mathbf{v}_i(t) + \frac{1}{2} \Delta t [\mathbf{a}_i(t) + \mathbf{a}_i(t + \Delta t)] \end{aligned} \quad \text{Equation 2.5}$$

where  $\Delta t$  represents the timestep associated with the simulation. Analogous expressions to Equation 2.5 can be derived for NVT and NPT equations of motion. Note that the accelerations of each atom,  $\mathbf{a}_i(t)$ , are determined via a force evaluation, based on atom positions, using the interatomic potential described in Section 2.5. LAMMPS [43] incorporates only the velocity-Verlet algorithm as it is more computationally efficient than some other common alternative solution algorithms (leapfrog, Runge-Kutta, and Verlet) because it requires only one force evaluation per iteration and explicitly determines the atom positions and velocities at each iteration step (rather than on  $\frac{1}{2}$  steps as is done in some other solution algorithms).

## 2.6 References

- [43] Plimpton S 1995 Fast Parallel Algorithms for Short-Range Molecular-Dynamics *J. Comput. Phys.* **117** 1–19
- [44] Germann T, Kadau K and Lomdahl P 2005 25 Tflop/s multibillion-atom molecular dynamics simulations and visualization/analysis on BlueGene/L *Proc. IEEE/ACM Supercomput.* 1–13
- [45] Kadau K, Lomdahl P S, Germann T C, Alder B and Wainwright T 2006 Molecular Dynamics Comes of Age: 320-Billion-Atom Simulation on BlueGene/L *Int. J. Mod. Phys. c* **17** 1755–61
- [46] Steinhauser M O and Hiermaier S 2009 A Review of Computational Methods in Materials Science: Examples from Shock-Wave and Polymer Physics *Int. J. Mol. Sci.* **10** 5135–216
- [47] Angelo J E, Moody N R and Baskes M I 1995 Trapping of hydrogen to lattice defects in nickel *Model. Simul. Mater. Sci. Eng.* **3** 289–307
- [48] Metropolis N, Rosenbluth A W, Rosenbluth M N, Teller A H and Teller E 1953 Equation of State Calculations by Fast Computing Machines *J. Chem. Phys.* **21** 1087
- [49] Haile J M 1992 *Molecular Dynamics Simulation* (New York: Wiley)
- [50] Frenkel, Daan, Smit B 2001 *Understanding Molecular Simulation: From Algorithms to Applications* (Academic press)
- [51] Shewchuk J R 1994 An Introduction to the Conjugate Gradient Method Without the Agonizing Pain *Science (80-. )*. **49** 64
- [52] Shinoda W, Shiga M and Mikami M 2004 Rapid estimation of elastic constants by molecular dynamics simulation under constant stress *Phys. Rev. B* **69** 134103
- [53] Hoover W G 1985 Canonical dynamics: Equilibrium phase-space distributions *Phys. Rev. A* **31** 1695–7

# CHAPTER 3: IMPLEMENTATION AND APPLICATION OF THE ATOMISTIC COHESIVE ZONE VOLUME ELEMENT APPROACH TO THE LATERAL TWIN GRAIN BOUNDARY SYSTEM

## 3.1 Steady-State Crack Propagation Simulation Model

The simulation approach in this study is based on a molecular dynamics (MD) model of crack propagation under time-independent, or steady-state, conditions along a flat grain boundary. The approach is composed of three steps: (i) creation of a hydrogenated grain boundary, (ii) introduction and propagation of an atomically sharp crack, and (iii) data mining to extract the relationship between atomistic simulations and continuum interface separation laws. Steps (i) and (ii) are covered in this section whereas the data mining procedure is discussed in Section 3.

### 3.1.1 Creation of Hydrogenated Grain Boundaries

The construction of a  $\Sigma 3(112)[1\bar{1}0]$  symmetric tilt grain boundary with varying concentrations of H at the primary grain boundary is done via a three-step process. First, the lowest energy  $\Sigma 3(112)[1\bar{1}0]$  symmetric tilt, hydrogen-free, grain boundary configuration is determined using a relatively small bicrystal system (<15,000 Ni atoms). To determine the minimum energy configuration, one grain is incrementally displaced relative to the other, sampling  $N_{pos}$  initial positions ( $N_{pos}=100$ ) within the grain boundary plane, and subjected to energy minimization using the Polak-Ribiere version of the nonlinear conjugate gradient algorithm [54]. The translation corresponding to the minimum energy configuration is used to

create larger systems utilized in the remainder of this study. The interface structure is consistent with prior work in the literature for the Ni  $\Sigma 3(112)[1\bar{1}0]$  grain boundary [55].

Second, using the translation associated with the minimum energy  $\Sigma 3(112)[1\bar{1}0]$  grain boundary structure, larger simulation models are created that are comprised of four layers following the methodology proposed by Yamakov et al. [37], as shown in Fig. 3.1: Two primary grains,

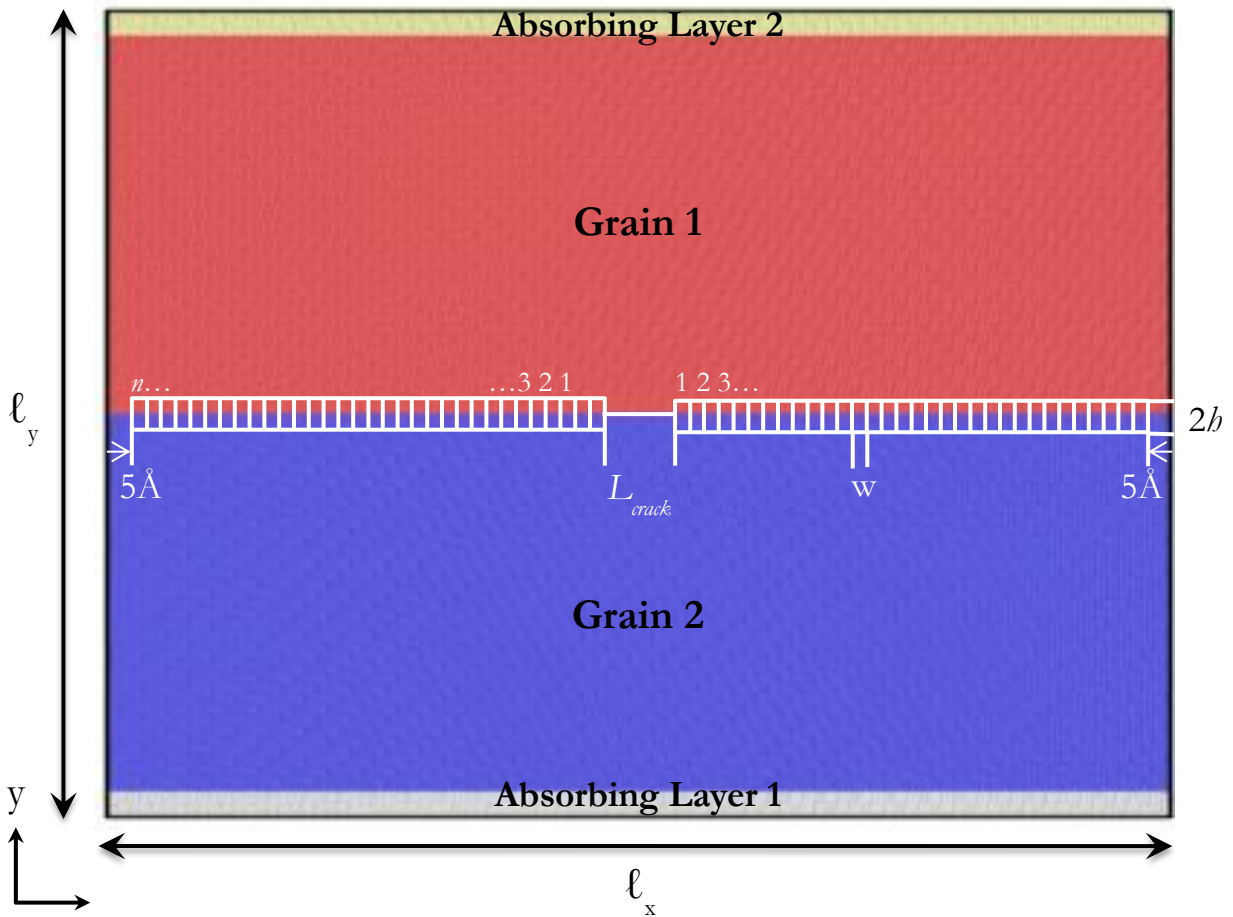


Figure 3.1. Schematic of the four layer crack-propagation model and cohesive zone volume element (CZVE) definition. The grain boundary between Grain 1 and Grain 2 is the primary grain boundary where the atomically sharp crack is introduced along with varying concentrations of hydrogen. The grain boundaries between Grain 1 and Absorbing Layer 2, Grain 2 and Absorbing Layer 1, and Absorbing Layer 1 and 2 all serve to ensure that dislocations emitted during crack propagation do not pass across the periodic boundaries causing the crack to interact with its own periodic image. Atoms within  $h$  of the primary grain boundary are assigned to CZVEs unless they fall within  $5 \text{ \AA}$  of the periodic boundary or within the region containing the atomically sharp crack,  $L_{crack}$ .

between which is the primary (hydrogenated) grain boundary, and two “absorbing layers” (hydrogen-free) on either side of the primary grains. The boundaries between the absorbing layers and the primary grains as well as the grain boundary between the two absorbing layers across the periodic boundary are referred to as “absorbing grain boundaries” and act as sinks to restrict dislocation movement through the periodic boundary. The dimensions of the atomistic system ( $\ell_x$ ,  $\ell_y$ , and  $\ell_z$ ) are chosen to be appropriate multiples of the grain boundary displacement shift complete distances [56], ensuring that no artificial boundaries or discontinuities are created as a result of the periodic boundary conditions. Specifically, for the lattice orientation in this manuscript, the simulation model  $\ell_x = 914.523 \text{ \AA}$ ,  $\ell_y = 1102.309 \text{ \AA}$  and  $\ell_z = 99.561 \text{ \AA}$  is selected containing approximately 9.39 million atoms. This simulation model size is sufficient so that the crack can propagate more than five times its initial length without self-image interactions through the periodic boundaries.

In the final step of the construction process, hydrogen atoms are added at the most energetically favorable atomic sites only within the primary grain boundary, thus generating a hydrogenated system in which H has completely segregated to the grain boundary. These sites and the equilibrium concentration of H for the  $\Sigma 3(112)[1\bar{1}0]$  grain boundary are predetermined using Monte Carlo simulations performed at 0 K [42] with the same interatomic potential as the current work. The Monte Carlo simulations were performed for 100,000 steps per atom where 50% of the steps attempted to add or remove H. These simulations determined that the equilibrium H concentration is approximately 300 appm for a chemical potential  $\mu = -2.35 \text{ eV}$  [42], which corresponds to a saturation grain boundary coverage of approximately  $0.132 \text{ H/\AA}^2$  (66.4% of favorable sites are populated with H). Figures 3.2(A) and 3.2(B) show the hydrogen-free grain boundary structure after energy minimization, while Figs. 3.2 (C) and (D) show the

three energetically favorable locations for H within the grain boundary from Monte Carlo simulations [42]. In the current work, 100% H saturation ( $0.198 \text{ H}/\text{\AA}^2$ ) refers to the configuration where every favorable site in each structural unit at the grain boundary is occupied by a H atom; 75% ( $0.149 \text{ H}/\text{\AA}^2$ ), 66.4% ( $0.132 \text{ H}/\text{\AA}^2$ ), 50% ( $0.099 \text{ H}/\text{\AA}^2$ ), and 25% ( $0.050 \text{ H}/\text{\AA}^2$ ) models are created by randomly removing H atoms from the fully populated (100% H saturation) grain boundary model. 0% H refers to a pristine hydrogen-free Ni grain boundary. Thus, the H grain boundary coverages examined in this work span the equilibrium grain boundary coverage determined via Monte Carlo simulations (over and under saturated with respect to thermodynamic equilibrium).

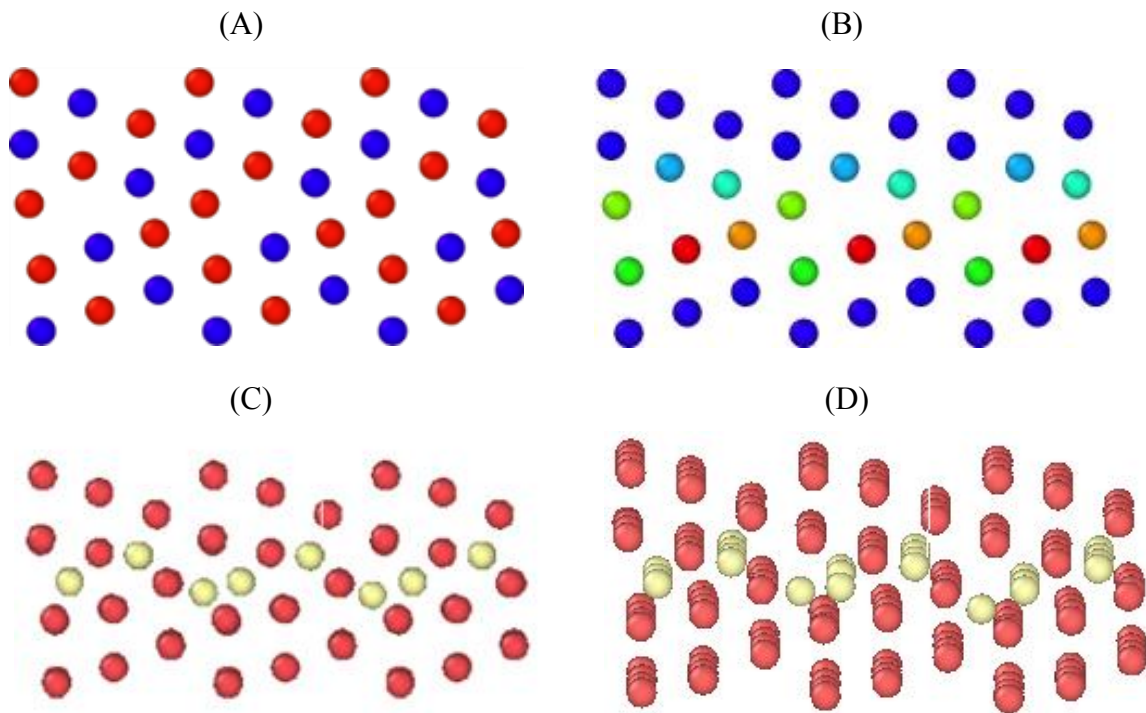


Figure 3.2. Structure of the primary  $\Sigma 3(112)[\bar{1}\bar{1}0]$  grain boundary. (A) and (B) Hydrogen-free minimum energy grain boundary structures colored by  $\{110\}$  atomic plane and the centrosymmetry parameter, respectively. (C) Projection along the misorientation axis and (D) rotated view of the grain boundary with H atoms (yellow) in the three most energetically favorable positions determined by Monte Carlo simulations. [42]



### 3.1.2 Steady-State Crack Propagation

Once the hydrogenated grain boundary model is constructed with a desired H coverage, the four-layer grain boundary system is relaxed via energy minimization using the Polak-Ribiere version of the nonlinear conjugate gradient algorithm [54] for 5,000 iterations to allow the grain boundary structure to accommodate the added H. Then, the temperature of the system is equilibrated to 300 K under a predefined hydrostatic tension,  $\sigma_H$ , for 100,000 ps in the isobaric-isothermal (NPT) ensemble, reaching equilibrium at the specified temperature and prestress. As a result, the hydrogenated grain boundary model is strained to provide a sufficient driving force for future crack propagation. In the case of the  $\Sigma 3(112)[11\bar{0}]$  symmetric tilt grain boundary,  $\sigma_H$  is set to 10 GPa based on preliminary simulations with various crack lengths. Dislocation emission is not observed under these hydrostatic prestress conditions. This general approach was initially developed to model steady-state crack propagation in pure Al by Yamakov et al. [37].

Once the system is equilibrated under the prestress conditions  $\sigma_H$ , the simulation is switched to an isovolume-isothermal (NVT) ensemble preserving the strain associated with the hydrostatic prestress. At this point, an atomically sharp crack of length  $L_{crack}$  is introduced in the center of the primary grain boundary, as shown in Fig. 3.1. The atomically sharp crack is introduced by screening the interactions between atoms in regions Grain 1 and Grain 2 only over the length  $L_{crack}$ . The screening remains active throughout the simulation. For the  $\Sigma 3(112)[11\bar{0}]$  symmetric tilt grain boundary in this work, the screened region is set to  $L_{crack} = 50 \text{ \AA}$  based on preliminary simulations to find a compatible combination of initial crack length and hydrostatic prestress appropriate for crack propagation. With the imposed strain due to the prestress  $\sigma_H$  and initial crack  $L_{crack}$ , the system is evolved for 40,000 ps which allows both crack tips (left and right directions) to propagate for approximately 100  $\text{\AA}$  in each direction along the plane of the

primary grain boundary. Simulations show that crack propagation and dislocation nucleation behavior are different for the left crack tip and the right crack tip. The role of  $H$  on this asymmetry will be examined in Section 3.3.

### 3.2 Extraction of Traction-Separation Behavior

Cohesive traction-separation relationships are extracted from atomistic forces and displacements ahead of each crack tip by tracking the evolution of the state of the CZVEs along the grain boundary during steady-state crack propagation. This approach has been successfully applied to pristine Al  $\Sigma$  99 bicrystals [37], results of which were reproduced to validate the implementation in this work. The influence of CZVE size, filtering approaches to deconvolute the elastic and decohesion response of the grain boundary, and the influence of different average techniques are explored in this section.

#### 3.2.1 Definition of Cohesive Zone Volume Elements (CZVE)

Before the atomically sharp crack is introduced via the screening approach described in Section 3.1.2, each atom within a distance  $h$  on either side of the primary grain boundary is assigned to a three-dimensional rectangular volume element (called a Cohesive Zone Volume Element), as shown in Fig. 3.1. The state of each CZVE at position  $x$  along the grain boundary and time  $t$  is defined by two state variables [54]: (i) the average normal stress,  $\sigma_{yy}(x,t)$ , computed using the virial definition [57], and (ii) the crack tip opening displacement,  $\lambda(x,t)$ . Thus, each CZVE state is represented as a point  $(\lambda, \sigma_{yy})$  in the  $\sigma$ - $\lambda$  configurational space at every snapshot in time. The average normal stress in a CZVE is computed using the volume of the CZVE which changes in time, effectively computing a true value of the average stress in each CZVE. An

analysis of the shape of the CZVE evolution has not been performed. Using a statistical mechanics approach, in the limit of steady-state crack propagation that occurs over an infinitely long time over an infinitely long interface, all realized CZVE states will produce a density of states distribution  $\rho(\lambda, \sigma)$  that is a continuous function independent of time. Via this approach, the decohesion behavior of the grain boundary is extracted as an average to mitigate the role of thermal vibrations and phonon wave propagation on the traction-separation relationship.

Specifically, the bounds of the CZVEs are determined by partitioning the prestressed system near the grain boundary into  $4n$  zones with  $2n$  zones above and  $2n$  zones below the primary grain boundary, resulting in  $n$  CZVE pairs along the left and right crack propagation directions. A  $5 \text{ \AA}$  region near each periodic boundary is omitted in the assignment of cohesive zones as some atoms may pass across the periodic boundary during the simulation and thus potentially affect the averaging of the center of mass of the outermost cohesive zones. This does not affect the traction-separation results as the crack does not propagate to within  $300 \text{ \AA}$  of the periodic boundary. Also, cohesive zones above/below the initial  $50 \text{ \AA}$  crack are omitted and not used to determine the average traction-separation relationship as they are within the screening length. The crack tip opening displacement,  $\lambda$ , is computed by tracking the change in the  $y$ -position of the center of mass of two vertically neighboring cohesive zones (normal to the grain boundary plane) as the crack propagates. This work focuses only on normal displacement during crack propagation and does not consider tangential displacements. A systematic survey was performed to determine the necessary size of each CZVE. Results, shown in Fig. 3.3, indicate that if the CZVEs are too small, the density of states  $\rho(\lambda, \sigma)$  data is highly sensitive to thermal effects and dislocation activity due to the statistically insufficient number of atoms in each CZVE for averaging. Yet, if the CZVEs are too large, an insufficient number of  $(\lambda, \sigma)$  data points are

extracted resulting in improper statistics of the decohesion behavior of the crack tip. Thus, for the remainder of this work, 200 CZVE pairs (100 pairs on each side of the initial crack) with  $w=9.53 \text{ \AA}$  and  $h=20 \text{ \AA}$  and containing roughly 1,500 atoms in each CZVE are used to effectively mitigate thermal and phonon effects.

### 3.2.2 Deconvolution of Elastic and Decohesion Response

As the crack unzips along the grain boundary plane, the raw density of states data includes information related to the decohesion response of the grain boundary, but also data associated with non-decohesion behavior such as thermal oscillations and the elastic response of the grain boundary to the hydrostatic prestress. The extracted traction-separation relationships should correspond uniquely to the decohesion behavior of the grain boundary without bias from the imposed prestress.

As shown in Fig. 3.4, the raw  $(\lambda, \sigma)$  density of states represents four approximate regions corresponding to different positions of the CZVE pairs relative to the propagating crack tip. Region 1 roughly encompasses states corresponding to CZVE pairs sufficiently far away from the propagating crack tip to be unaffected or minimally affected by the plasticity ahead of the crack tip or the crack tip itself. Thus a majority of the states (low  $\lambda$ , high  $\sigma$ ) in Region 1 correspond to the elastic stiffness of the grain boundary. Region 2 encompasses states corresponding to CZVE pairs sufficiently close to the crack tip to be affected by the plasticity generated during propagation or containing the crack tip. Regions 3 and 4 encompass states corresponding to CZVE pairs through which the crack tip has propagated and are distinguished by the degree of separation; states of CZVE pairs in Region 3 have separated significantly but are not fully separated whereas states of CZVE pairs in Region 4 have fully separated.

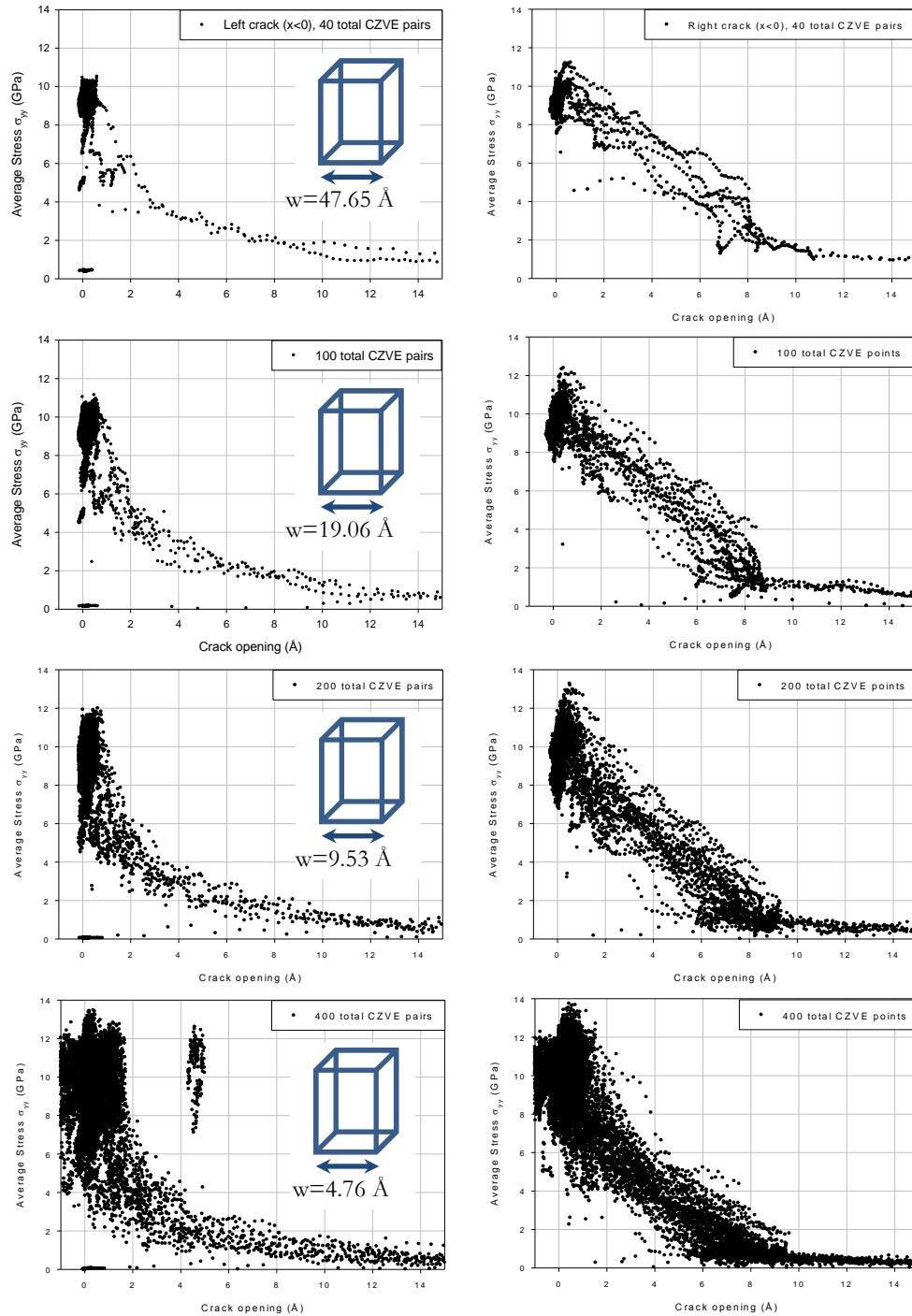


Figure 3.3. Traction-separation density of states,  $\rho(\sigma, \lambda)$ , for crack propagation to the left (left column) and right (right column) for a grain boundary with 25%H using 40 (row 1), 100 (row 2), 200 (row 3), and 400 (row 4) total CZVE pairs. Using 40 and 100 CZVE pairs results in data sparsely populated in some crack opening bands while using 400 CZVE pairs results in a density highly dependent on thermal vibrations, phonon wave propagation, and dislocation nucleation events.

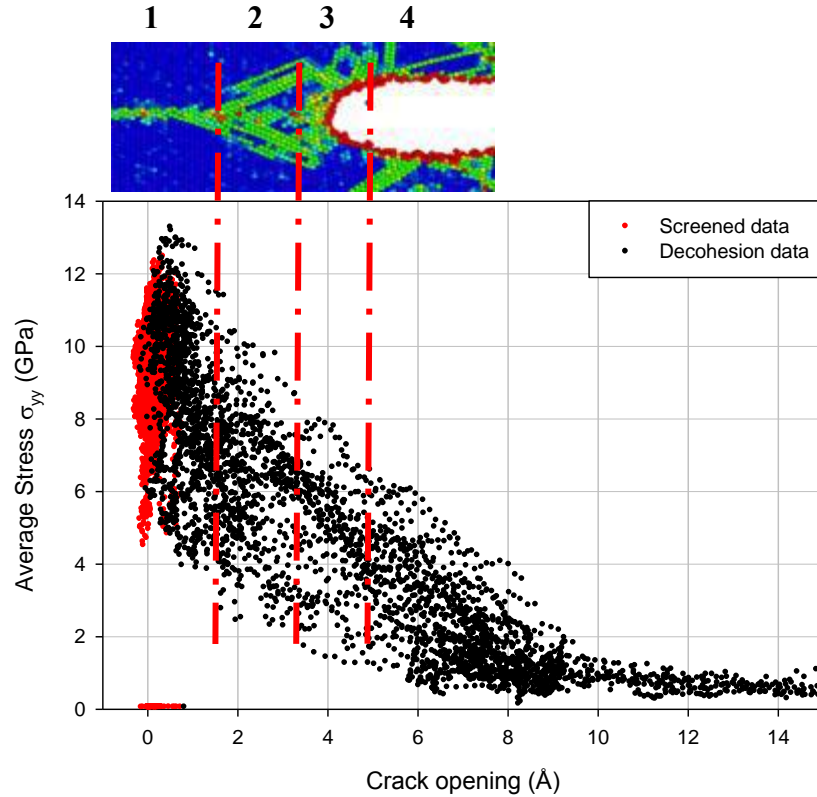


Figure 3.4. Anatomy of the traction-separation curve. Region 1 contains states corresponding to CZVE pairs far ahead of the crack tip to be unaffected by the plasticity ahead of the crack tip or the crack tip itself. Data points in Region 2 correspond to CZVE pairs significantly affected by the plasticity ahead of the crack tip or contain the crack tip. Data points in Region 3 correspond to separated CZVE pairs through which the crack tip has passed through but have not separated completely. Data points in Region 4 correspond to CZVE pairs far behind the crack tip that have significantly separated. The screened points, shown in red, are omitted when including 2 CZVE ahead of the left crack tip with 25% H coverage at the primary grain boundary.

To limit the set of  $(\lambda, \sigma)$  data to that exclusively associated with the decohesion response of the grain boundary, the density of states is filtered to include only CZVEs that are at or in the local neighborhood ahead of the propagating crack tip. To quantitatively track the position of the crack tip, a crack tip opening displacement threshold is defined, above which a cohesive zone pair is considered open, meaning that the crack is within or has propagated through this pair of cohesive zones. In this work, a cohesive zone pair is considered open if the normal opening displacement is greater than  $\delta=1.5 \text{ \AA}$ , as this is greater than the Burger's vector of a Shockley

partial dislocation in Ni ( $1.437 \text{ \AA}$ ) and thus the CZVE pair would not be considered open after a single partial dislocation emission event. Effectively, by screening all data points with opening displacements less than the  $1.5 \text{ \AA}$  opening criteria, the final traction-separation relationship is composed of points only in Regions 2, 3, and 4 in Fig. 3.4. Figure 3.5 shows traction-separation relationships including 0, 1, 2, and 3 CZVEs ahead of the crack tip (along with all opened CZVEs) in the density of states. In Figs. 3.5(C) and 3.5(D), a running average with  $M=250$  data points is used to generate the traction-separation curve from the density of states data. Through

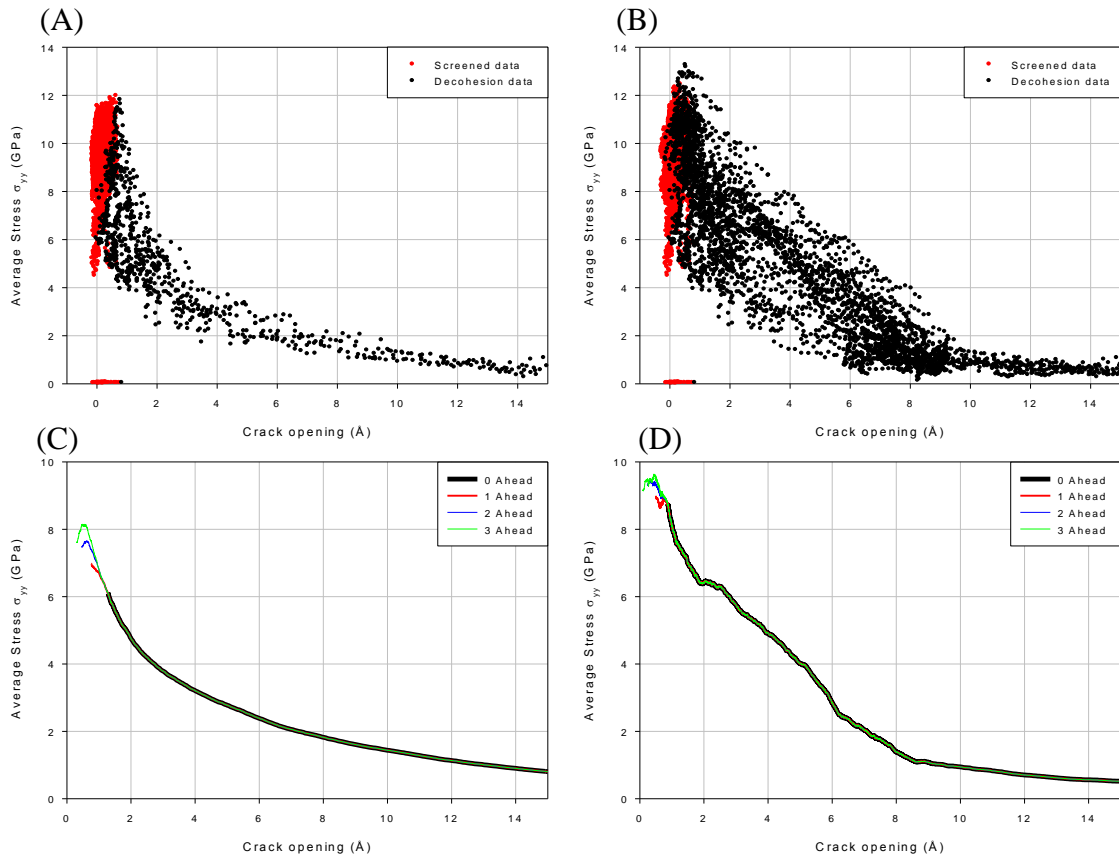


Figure 3.5. (A) and (B) Density of states for CZVEs located ahead of the left and right crack tips, respectively. Red data points correspond to screened elastic stiffness points when including 2 CZVE ahead of the propagating crack tips. (C) and (D) Survey of the effect of inclusion of different numbers of CZVEs ahead of propagating crack tip on the traction-separation relationship for both left (C) and right (D) crack tips for 25% H coverage at the grain boundary. All simulations are performed using 100 CZVE pairs ahead of each crack tip and plots are generated using a running averaging with  $M=250$  points.

this filtering approach, the  $(\lambda, \sigma)$  data points for CZVE pairs far ahead of the crack tip, a majority of which remain at equilibrium at the hydrostatic prestress of 10 GPa (states in Region 1 of Fig. 3.4), are excluded from the grain boundary decohesion relationship. Using this simple comparative sensitivity analysis, it is concluded that data from 2 CZVE pairs ahead of the crack tip should be utilized. The combined effect of only including data from open CZVE pairs and 2 unopened CZVE pairs ahead of the crack tip, while not including data from CZVE bordering free surfaces or the periodic boundary, ensures that the traction-separation relationship corresponds to the decohesion behavior of the grain boundary with limited effects of the grain boundary elastic stiffness or other physical mechanisms.

### 3.2.3 Influence of Averaging Scheme on Traction-Separation

The state of each cohesive zone volume element  $(\lambda, \sigma_{yy})$  is computed at a constant time interval  $\Delta t = 250$  ps during crack propagation. After generating the density of states, a curve fit is applied to the deconvoluted traction-separation data. As a part of this study, the results of two averaging techniques are analyzed to determine which method provides the best average representation of the density of states  $\rho(\lambda, \sigma)$  over a wide range of crack tip opening displacements. The first averaging technique fits a piece-wise linear curve to the filtered traction-separation data by dividing the range of crack tip opening displacements into  $N$  equally spaced bins, representing a small interval  $(\lambda - \Delta\lambda, \lambda + \Delta\lambda)$ , over which the traction and crack tip opening displacements are averaged resulting in a single data point for every one of the  $N$  bins. A survey of the effect of the averaging bin size on the traction-separation relationship is provided in Fig. 3.6(A) for propagation of the left crack tip. The second averaging technique fits a piece-wise linear curve to the filtered traction-separation data using a running average technique.



Specifically, the first point in the running average is computed by averaging the first  $M$  ( $\lambda, \sigma_{yy}$ ) values. Each subsequent point in the running average is generated by shifting the range of  $M$  points by 1. A survey of the effect of the number of points  $M$  employed in the running average on the traction-separation relationship is shown in Fig. 3.6(B) for propagation of the left crack tip.

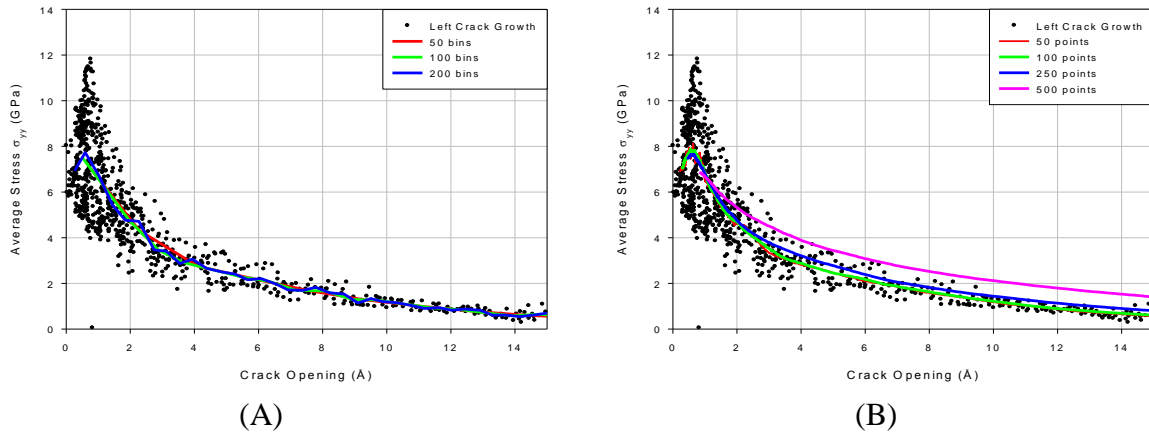


Figure 3.6. Survey of the effect of averaging methodology on the extracted traction-separation curves using filtered data for propagation of the left crack tip with 25% H coverage: (A) survey of bin size effects (B) survey of running average parameter,  $M$ , effects.

Based on these results, the running average technique with  $M=250$  is chosen as the most appropriate technique to extract a smooth traction-separation relationship while accurately capturing the peak and the shape of the density of states data. One of the limitations of the binning approach is that each bin contains an inconsistent number of data points; bins associated with small opening displacements represent many more CZVE states than bins associated with large opening displacements. Average points generated using the binning technique are highly sensitive to the number of points in the binning region. Alternatively, the running average technique is preferred over the binning average technique as it is able to capture a clear maximum in the traction-separation relationship while representing a uniform number of CZVE

states. Note, Fig. 6 shows data for crack propagation in the left direction, these conclusions are consistent for the analysis of crack propagation in the right direction for the  $\Sigma 3(112) [1\bar{1}0]$  grain boundary.

### 3.3 Role of H on Intergranular Embrittlement

The outlined numerical methodology in Sections 3.1 and 3.2 to extract the traction-separation relationship from  $\rho(\sigma, \lambda)$  is applied to the  $\Sigma 3(112)[1\bar{1}0]$  grain boundary in Ni with systematically varying H coverage at the primary grain boundary to explore the effect of H coverage on the traction-separation relationship. Insights on the atomistic mechanisms such as HELP and HID in the vicinity of the crack tip and their relation with the work of separation are discussed in this section.

#### 3.3.1 Crack Tip Plasticity

A qualitative analysis of left and right crack tips during steady-state crack propagation shows that varying the coverage of H at the grain boundary influences the structure of the grain boundary and dislocation emission from the crack tip. Figure 3.7 shows the atomistic region around the propagating crack after 10,000 ps with different coverage amounts of H at the primary grain boundary. First, it is clear that the structure of the grain boundary is modified by the presence of hydrogen. Indeed, in Fig. 3.7(A) the discrete extended stacking faults associated with the hydrogen free grain boundary structure in the vicinity of the crack tips are observable, while in Fig. 3.7(E) the 100% saturated grain boundary structure identified via centrosymmetry is more uniform along the grain boundary plane with a finite thickness. Second, due to the crystallographic orientation of each lattice relative to the left and right crack tips, asymmetric

dislocation nucleation occurs. The left crack tip emits the same twin dislocation in all systems whereas the density and type of dislocations nucleated from the right crack tip varies with H coverage. Figure 3.7 qualitatively shows that dislocation nucleation is at a maximum for steady-state crack propagation along the hydrogen-free grain boundary and at a minimum for either the 50% H or 66.4% H grain boundary model. This variability may be due to the randomness associated with the sites occupied by the H atoms added to the vicinity of the primary grain boundary. Finally, it is noteworthy to observe that the 66.4% H coverage corresponds to the equilibrium saturated state of the  $\Sigma 3(112)[1\bar{1}0]$  grain boundary predicted from Monte Carlo calculations.

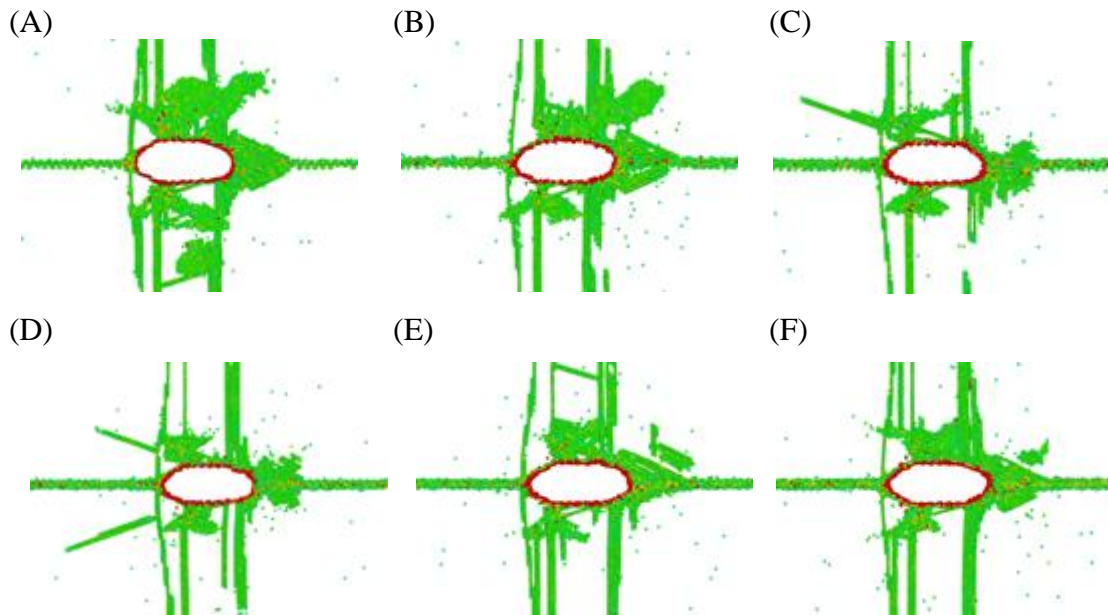


Figure 3.7. Dislocation activity during crack propagation colored by the centrosymmetry parameter at 10,000 ps with (A) 0%, (B) 25%, (C) 50%, (D) 66.4%, (E) 75%, and (F) 100% H coverage at the primary grain boundary. Hydrogen saturation at the grain boundary influences both the structure of the grain boundary and dislocation nucleation during crack propagation.

### 3.3.2 Decohesion Behavior

The quantitative effect of varying H coverage at the primary grain boundary is discussed in terms of the crack tip velocity during propagation, the work of separation of the grain boundary, and the peak stress of the extracted traction-separation relationships.

First regarding the crack tip velocity, recall, the crack tip position and associated velocity are identified by tracking the center of mass position of vertically neighboring pairs of CZVEs along the grain boundary. As shown in Fig. 3.8, the crack tip velocity, computed by linearly interpolating the crack tip position data as a function of time, shows asymmetry depending on the crack propagation direction (Table 3.1). As illustrated in Fig. 3.8(B), when propagating to the left (-x direction), the crack tip velocity generally increases with increasing H concentration. However, when propagating to the right (+x direction), the crack tip velocity generally decreases with increasing H concentration. Interestingly, the crack tip velocities are converging towards each other as H coverage is increased at the primary grain boundary. This is rationalized by examining the structure of the grain boundary ahead of the each crack tip, as shown in Fig. 3.7. As observed in Section 3.3.1, hydrogen promotes a more uniformly distorted grain boundary structure, mitigating both the influence of the orientation of the extracted stacking faults (Fig. 7(A)) and the orientation of the structural units relative to the activated slip systems in each lattice. Finally, note that both left and right crack tip velocities are reasonably constant over the simulation time, supporting the assumption of steady-state crack propagation necessary for extracting decohesion relationships.

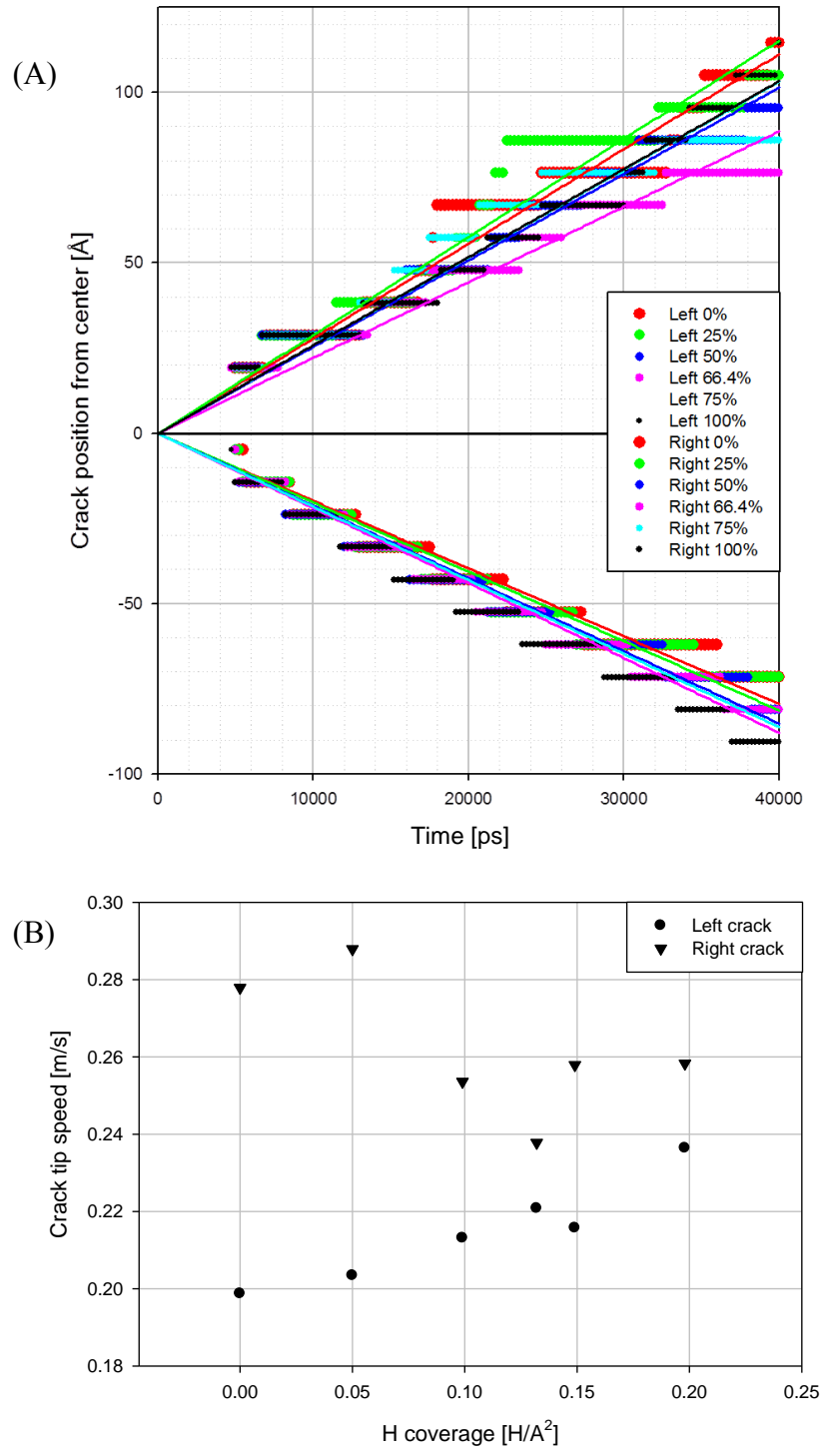


Figure 3.8. (A) Crack tip position as a function of time. Propagation of the right crack tip is positive and propagation of the left crack tip is negative relative to the grain boundary model coordinate system, The data for 66.4% coverage corresponds to the simulation shown in Fig. 7. (B) Crack tip speed as a function of H coverage. The left and right crack tip speeds for the 66.4% coverage case are the average values of the three simulations that were performed.

Second, as illustrated in Figs. 3.9 and 3.10, the peak stress shows a general decrease with increasing H coverage at the primary grain boundary (data provided in Table 3.1). An exception to this is the half-saturated (50% H) grain boundary which shows a slight increase in the peak stress.

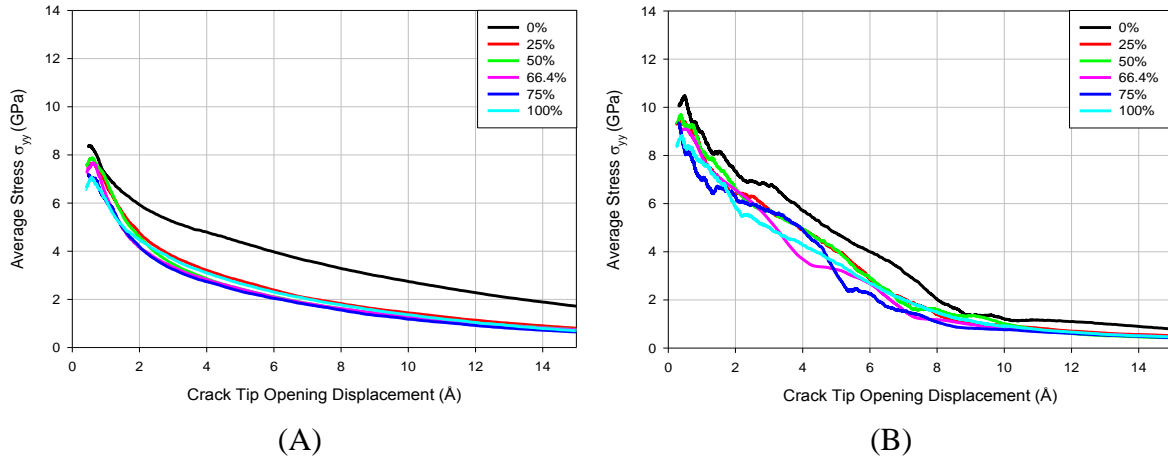


Figure 3.9. Role of H saturation on traction-separation curves of (A) left (-x direction) and (B) right (+x direction) crack tips. All simulations are performed using 100 CZVE ahead of each crack tip and plots generated using running average technique with  $M=250$  points. The plots for the 66.4% H coverage case correspond to the simulation shown in Fig. 3.7.

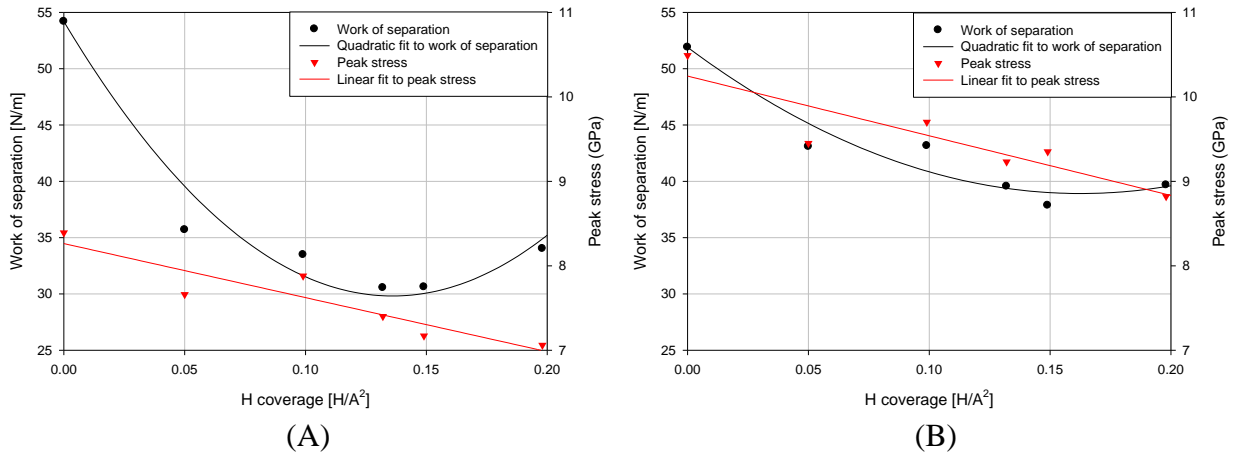


Figure 3.10. Dependence of the work of separation and peak stress as a function of H coverage for propagation of the (A) left (-x direction) and (B) right (+x direction) crack tips. The values for peak stress and work of separation for both the left and right crack tips for the 66.4% coverage case are the average values of the three simulations that were performed. Quadratic and linear fits are provided to illustrate general trends and not meant to indicate a specific mechanism.

Finally, the work of separation (the work required to separate the grain boundary into two free surfaces) can be computed by integrating the traction-displacement curve (a maximum opening displacement of 15 Å is selected for this integration). As shown in Fig. 3.10, the work of separation generally decreases with increasing H saturation until a minimum is reached around the equilibrium H saturation of 66.4% H coverage. Then, the work of separation modestly increases for the 100% H coverage which is severely oversaturated compared to equilibrium determined by Monte Carlo calculations.

It is understood that statistical variability exists within molecular dynamics simulations. To assess the extent of this variability, three simulations with different random realizations of H coverage at the grain boundary and different random initialized thermal velocities have been conducted. The standard deviations associated with the computed values for peak stress and work of separation are presented in Table 3.1 and show that statistical variability has little impact on the observed trends for peak stress and work of separation as a function of H coverage.

The left crack tip nucleates the same twinning dislocation during crack propagation, regardless of H saturation; yet, the velocity of the crack increases and the work of separation and peak strength decrease with increasing H coverage. These observations are consistent with the theory of the HID mechanism, and are consistent with prior results for low H coverages [58]. Plasticity nucleating from the right crack tip appears to decrease as H coverage increases from 0% H to 66.4% H (equilibrium saturation) and then begins to increase as H coverage increases from 66.4% H to 100% H, with different slip systems activated at different concentrations of H (Fig. 3.7). Thus, for this propagation direction a combination of HID and HELP may be more appropriate to describe crack propagation depending on the deviation of the grain boundary from equilibrium H saturation. A more detailed analysis of the dislocation emission processes from the

$\Sigma 3(112)[1\bar{1}0]$  is necessary before a quantitative comparison can be made to previous results showing that low concentrations of H facilitated dislocation emission at a crack tip [28,59].

	<b>0% H Coverage</b>	<b>25% H Coverage</b>	<b>50% H Coverage</b>	<b>66.4% H Coverage</b>	<b>75% H Coverage</b>	<b>100% H Coverage</b>
	<b>0.000 H/ Å<sup>2</sup></b>	<b>0.050 H/ Å<sup>2</sup></b>	<b>0.099 H/ Å<sup>2</sup></b>	<b>0.132 H/ Å<sup>2</sup></b>	<b>0.149 H/ Å<sup>2</sup></b>	<b>0.198 H/ Å<sup>2</sup></b>
<b>Left Crack Tip</b>						
<b>Crack Tip Velocity [m/s]</b>	0.1987	0.2034	0.2131	0.2208 ± 0.007	0.2157	0.2364
<b>Peak Stress [GPa]</b>	8.39	7.66	7.88	7.40 ± 0.27	7.17	7.06
<b>Work of Separation [N/m]</b>	54.19	35.69	33.48	30.55 ± 2.239	30.62	34.02
<b>Right Crack Tip</b>						
<b>Crack Tip Velocity [m/s]</b>	0.2779	0.2879	0.2536	0.2378 ± 0.0257	0.2579	0.2583
<b>Peak Stress [GPa]</b>	10.49	9.45	9.70	9.23 ± 0.13	9.35	8.82
<b>Work of Separation [N/m]</b>	51.90	43.08	43.16	39.55 ± 1.552	37.86	39.67

Table 3.1. Crack tip velocity and work of separation for both crack tips at all saturation levels simulated. Crack tip velocity is determined by fitting a line to crack tip propagation data; peak stress is determined using  $M=250$  running average technique to extract traction-separation relationship; work of separation is computed using a numerical integration technique.

### 3.4 References

- [28] Daw M S, Baskes M I, Bisson C L and Wolfer W G 1986 Application of the Embedded Atom Method to Fracture, Dislocation Dynamics, and Hydrogen Embrittlement. *Modeling Environmental Effects on Crack Growth Processes. Proceedings of a Symposium Held at the 1985 Fall Meeting of the Metallurgical Society.* (Sandia Natl Lab, Livermore, CA, USA, Sandia Natl Lab, Livermore, CA, USA: Metallurgical Soc of AIME) pp 99–124
- [37] Yamakov V, Saether E and Glaessgen E H 2008 Multiscale modeling of intergranular fracture in aluminum: Constitutive relation for interface debonding *J. Mater. Sci.* **43** 7488–94



- [42] O'Brien C J and Foiles S M 2014 *Private Communication*
- [54] Polak E and Ribiere G 1969 Note sur la convergence de méthodes de directions conjuguées *ESAIM Math. Model. Numer. Anal. - Modélisation Mathématique Anal. Numérique* **3** 35–43
- [55] Baskes M I, Sha X, Angelo J E and Moody N R 1999 Trapping of hydrogen to lattice defects in nickel *Model. Simul. Mater. Sci. Eng.* **5** 651–2
- [56] Bollmann W 1970 *Crystal defects and crystalline interfaces* (Springer)
- [57] Tsai D H 1979 The virial theorem and stress calculation in molecular dynamics *J. Chem. Phys.* **70** 1375
- [58] Hoagland R G and Heinisch H L 1992 Atomic simulation of the influence of hydrogen on the fracture behavior of nickel *J. Mater. Res.* **7** 2080–8
- [59] Li Z, Li J, Chu W, Liu H and Qiao L 2002 Molecular Dynamics Simulation and Experimental Proof of Hydrogen-enhanced Dislocation Emission in Nickel *J. Univ. Sci. Technol. Beijing Miner. Metall. Mater. (Eng Ed)* **9** 59–64

CHAPTER 4: APPLICATION OF THE ATOMISTIC COHESIVE ZONE VOLUME  
ELEMENT APPROACH TO GRAIN BOUNDARIES VICINAL TO THE COHERENT TWIN

In this chapter, the atomistic cohesive zone volume element approach for extracting the decohesion relationship of a grain boundary is applied to study steady-state crack propagation along two grain boundaries that have small-angle misorientations from the vicinal twin  $\Sigma 3(111)$  grain boundary. The purpose of simulating these nearly coherent grain boundaries is to demonstrate the robustness of the methodology implemented and validated in Chapter 3 to extract the traction-separation curves and associated properties for virtually any grain boundary system with or without the inclusion of atomic hydrogen segregated to the grain boundary.

4.1 Significance of the Grain Boundaries Near to the Vicinal Twin

Two grain boundaries are chosen with misorientations near that of the symmetric tilt coherent twin  $\Sigma 3(111)[1\bar{1}0]$  grain boundary. These two grain boundaries have misorientations about the  $\langle 110 \rangle$  misorientation axis less than ( $100.52^\circ$  defined as “interior”) and greater than ( $119.6^\circ$  defined as “exterior”) the  $109.5^\circ$  misorientation associated with the coherent twin grain boundary. The lattice orientations for the interior, coherent, and exterior grain boundaries are provided in Table 4.1. The selected grain boundaries have dissimilar disconnection structures

	Interior		Coherent		Exterior	
	Grain 1	Grain 2	Grain 1	Grain 2	Grain 1	Grain 2
x	$[-10-10-17]$	$[-10-10 17]$	$[-1-12]$	$[11-2]$	$[-7 -7 -17]$	$[-7 -7 17]$
y	$[17 17 -20]$	$[-17 -17 -20]$	$[111]$	$[111]$	$[17 17 -14]$	$[-17 -17 -14]$
z	$[1-1 0]$	$[1-1 0]$	$[-110]$	$[1-1 0]$	$[1 -1 0]$	$[1-1 0]$

Table 4.1. Lattice orientations used to model the interior, coherent twin, and exterior grain boundaries. The designations of Grain 1 and Grain 2 are consistent with the convention put forth in Chapter 3 in Figure 3.1.

along the interface plane. The structural differences of these three grain boundaries can be seen in Fig. 4.1. The structure of the interior ( $100.52^\circ$ ) grain boundary is characterized by compact core disconnections at 300 K, as shown in Fig. 4.1(A). The structure of the exterior ( $119.6^\circ$ ) grain boundary is characterized by disconnections that dissociate and emit extended stacking faults which alternate on either side of the grain boundary, as shown in Fig. 4.1 (C). In comparison, the  $\Sigma 3$  coherent twin grain boundary does not contain disconnections along the grain boundary plane and is perfectly mirror-symmetric, as shown in Fig. 4.1(B).

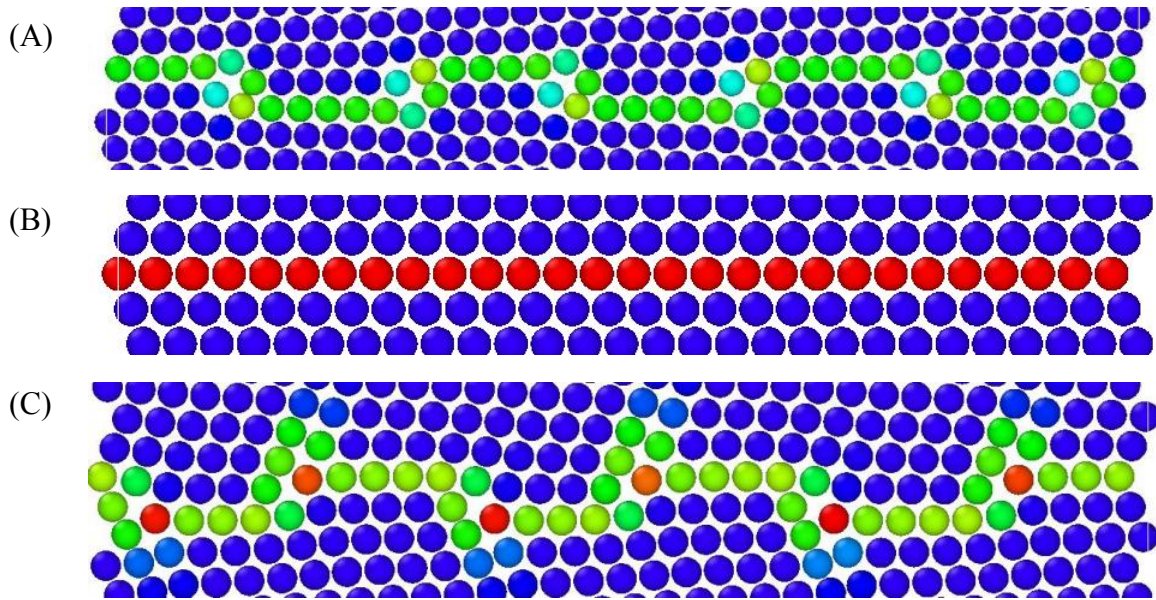


Figure 4.1. Grain boundary structures for the interior (A), coherent twin (B), and exterior (C) grain boundaries. Atoms are colored by centrosymmetry, which is a measure of the perfectness of the surrounding lattice structure. In this figure, propagation to the left is in the negative x-direction and propagation to the right is in the positive x-direction.

In addition to structural differences along the grain boundary plane, the two selected grain boundaries differ in the orientation and character of the slip planes that would be activated by a tensile stress applied normal to the grain boundary. For the exterior grain boundary, the primary slip systems for this lattice orientation when subjected to a uniaxial load normal to the grain boundary are co-planar with the misorientation axis for the grain boundary parallel to the

primary slip plane. Thus, the primary dislocations in this model (when subjected to a uniaxial load normal to the boundary) are parallel to the simulation cell misorientation axis. On the other hand, the interior boundary would have primary slip systems during uniaxial loading that are not coplanar nor are they aligned with the misorientation axis for the grain boundary. Thus, if the dislocations are emitted on primary slip systems, the dislocations are at obtuse angles to the simulation cell axes. Dislocation emission on non-primary slip planes for the interior grain boundary is reasonable, though, because the computed Schmid Factor for slip on the slip planes oriented parallel to the misorientation axis is about 60-70% of the value for the primary slip systems. Further, the stress state around the crack tip is complex (not uniaxial), so a Schmid Factor calculation is an over-simplification of the problem.

#### 4.2 Creation of Hydrogenated Grain Boundary Systems

The interior and exterior misoriented grain boundary models are generated via the methodology described in Section 3.1.1. The four-layer interior grain boundary model has dimensions  $\ell_x = 934.067 \text{ \AA}$ ,  $\ell_y = 1100.811 \text{ \AA}$  and  $\ell_z = 99.558 \text{ \AA}$  and contains approximately 9.39 million atoms. The four-layer exterior grain boundary system has dimensions  $\ell_x = 831.499 \text{ \AA}$ ,  $\ell_y$

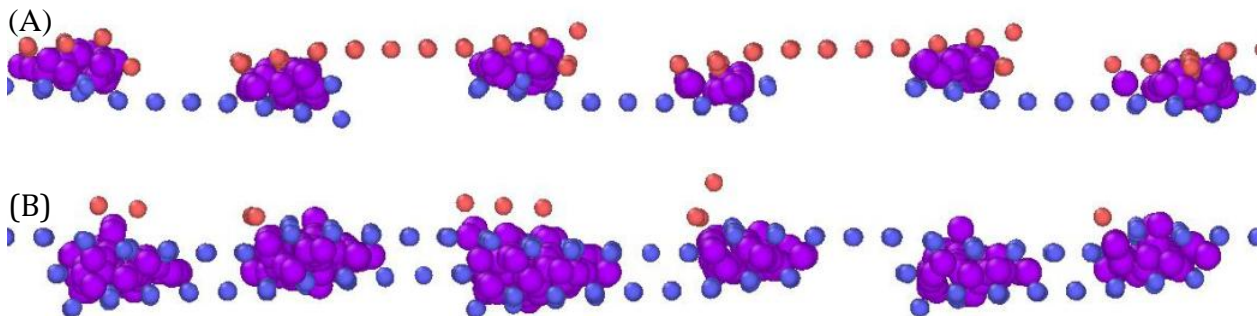


Figure 4.2. Energetically favorable positions for H (purple) atoms to occupy within the interior (A) and exterior (B) Ni (red and blue atoms) grain boundaries. The H coverages shown correspond to the 100% saturation case. The H atoms tend to segregate to the disconnection cores (A) and stacking faults (B).

= 1077.226 Å and  $\ell_z = 99.558$  Å and contains approximately 8.17 million atoms. Monte Carlo simulations determined that the equilibrium H coverage for a chemical potential  $\mu = -2.35$  eV [42] is approximately 0.102 H/Å<sup>2</sup> and 0.161 H/Å<sup>2</sup> for the interior and exterior grain boundary systems, respectively. Using a nearly identical procedure as that described in Chapter 3, hydrogen atoms are added to the most energetically favorable positions within the grain boundary, again, guided by Monte Carlo simulation results. Because hydrogen atoms do not occupy three discrete locations in the interior and exterior grain boundaries, the energetic insertion criteria is relaxed slightly to allow H atoms to occupy sites that may correspond to higher energy positions. In this chapter, the number of H atoms added to the grain boundary is chosen to span the equilibrium concentration for each respective grain boundary. In both cases hydrogen is added in six concentrations: 0%, 50%, 75%, 100%, 125%, and 150%, where 0% refers to the pure nickel grain boundary system and 100% refers to the grain boundary saturated with the equilibrium concentration of hydrogen as determined by Monte Carlo simulations for the chosen chemical potential [42]. The interior and exterior grain boundaries saturated with 100% H are shown in Fig. 4.2, which illustrates that the H atoms tend to localize to the areas with the greatest amount of free volume, i.e. the disconnection cores in the interior grain boundary (Fig. 4.2(A)) and the stacking faults in the exterior grain boundary (Fig. 4.2(B)).

### 4.3 Steady-State Crack Propagation

The interior and exterior grain boundary models, both with and without hydrogen at the primary grain boundary, are equilibrated using the same methodology that is detailed in Section 3.1.2, with only minor changes made to certain parameters. Specifically, both systems are equilibrated to a temperature of 300 K under a predefined hydrostatic tension  $\sigma_H$  of 8 GPa for

140,000 ps in the isobaric-isothermal (NPT) ensemble. A hydrostatic tension of 8GPa is necessary as higher stresses cause extension of the stacking faults in the exterior grain boundary models whereas lower stresses (4, 5, 6, and 7 GPa) did not provide sufficient driving force for crack propagation to occur in either system. Additionally, the screened region generating the atomically sharp crack is set to be  $L_{crack} = 150 \text{ \AA}$  based on preliminary simulations to find a compatible combination of initial crack length and hydrostatic prestress appropriate for crack propagation. Finally, with the imposed strain due to the 8 GPa hydrostatic prestress and 150  $\text{\AA}$  initial crack, the interior grain boundary model is evolved for 35,000 ps, while the exterior grain boundary model is evolved for 25,000 ps which allows the crack tips to propagate for between approximately 45-80  $\text{\AA}$  in each direction along the plane of the primary grain boundary. The exterior grain boundary model is evolved for a shorter time because the region of stacking faults extending from the grain boundary ahead of one crack tip begin to intersect the region ahead of the other crack tip across the periodic boundary leading to image force effects early in its evolution. In either case, the extent of crack propagation is sufficient for extraction of the traction-separation relationships via the methodology described in Section 3.2.

#### 4.4 Decohesion Behavior

The qualitative role of H segregated to the grain boundary is assessed through analysis of the physical output of the molecular dynamics simulations of steady-state crack propagation. Qualitatively, the decohesion behavior is assessed through the extraction of traction-separation relationships from grain boundaries with misorientations interior or exterior to the  $\Sigma 3(111)[1\bar{1}0]$  symmetric tilt coherent grain boundary. The quantitative effect of varying H coverage at the

primary grain boundary is discussed in terms of the work of separation of the grain boundary and the peak stress of the extracted traction-separation relationships.

Figure 4.3 shows the dislocation activity around each crack tip during the crack propagation process. The extent of crack propagation along both the interior and exterior grain boundaries exhibits a strong dependence on the propagation direction, as was the case with the lateral twin

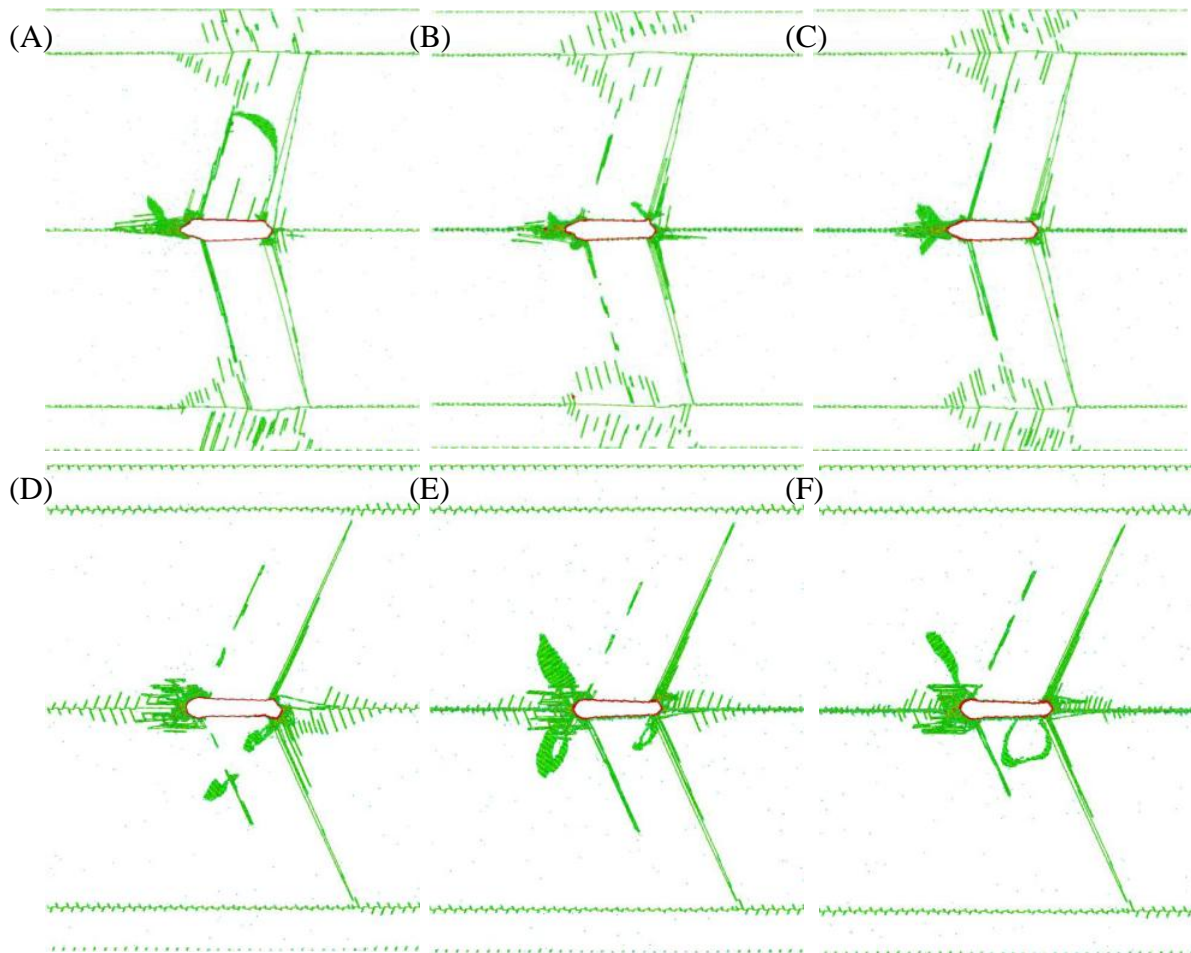


Figure 4.3. Dislocation activity during crack propagation colored by the centrosymmetry parameter. The top row of figures correspond to the interior grain boundary system at 20,000 ps with 0% H (A), 100% H (B) and 150% H (C) coverages at the primary grain boundary. Similarly, the bottom row of figures correspond to the exterior grain boundary system at 15,000 ps with 0% H (D), 100% H (E) and 150% H (F) coverages at the primary grain boundary. Hydrogen saturation at the grain boundary influences both the structure of the grain boundary and dislocation nucleation during crack propagation.

grain boundary studied in Chapter 3. During crack propagation along the interior grain boundary, the right crack tip nucleates twin dislocations and the left crack tip emits partial dislocations and encounters significant localized dislocation activity ahead of the propagating crack tip, as shown in Figs. 4.3 (A-C). Similarly, during crack propagation along the exterior grain boundary, twin dislocations are nucleated from the right crack tip and dislocations localize ahead of the left crack tip where partial dislocations are also emitted. Although it is not evident to what extent the inclusion of hydrogen affects the amount or types of dislocations present in the interior grain boundary system, the effect of hydrogen segregation is clearly evident in the exterior grain boundary system. The increasing coverage of hydrogen at the exterior grain boundary hinders the extension of partial dislocations with the connected stacking fault from the primary grain boundary, although the amount of dislocation density nucleated from the crack tips does not seem to change. These partial dislocations with connected stacking faults are visualized using centrosymmetry as parallel defects extending from the primary grain boundary into the bulk, most prominently in the system with 0% H (Fig. 4.3 (D)) and least prominently in the system with 150% H (Fig. 4.3 (F)).

The result of the differing energy dissipation mechanisms ahead of the crack tips during propagation is manifested in the extracted traction-separation curves and associated mechanical properties, provided in Fig. 4.4 and Figs. 4.5-4.6, respectively. Figure 4.4 shows the traction-separation curves for both the interior (Fig. 4.4 (A-B)) and exterior (Fig. 4.4 (C-D)) grain boundaries with varying amounts of hydrogen in energetically favorable positions at the primary grain boundary. Directly comparing propagation of the left crack tips (Fig. 4.4 (A) or (C)) to the corresponding propagation of the right crack tip (Figs. 4.4 (B) or (D)) shows that the peak stress is larger for propagation of the left crack tips which nucleate the partial dislocations and



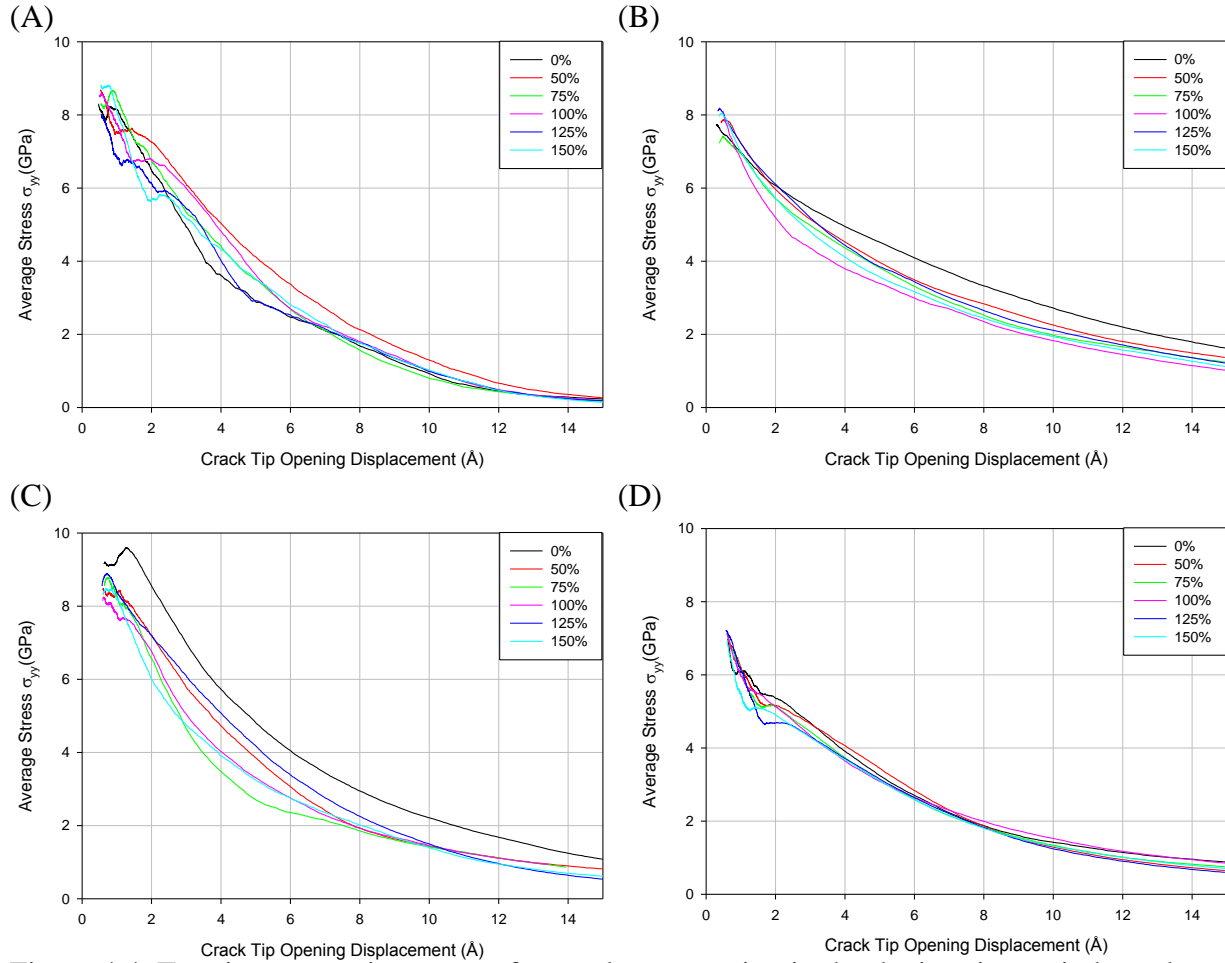


Figure 4.4. Traction-separation curves for crack propagation in the the interior grain boundary system [left (-x direction) (A); right (+x direction) (B)] and the exterior grain boundary system [left (-x direction) (C); right (+x direction) (D)].

encounter significant localized dislocation activity. This is also reflected in Figs. 4.4-4.5 and Tables 4.1-4.2. However, a higher peak stress does not guarantee a higher work of separation (area under traction-separation curve) during propagation. During propagation along the interior grain boundary, the left crack tip requires a lower work of separation but experiences a higher peak stress than propagation of the right crack tip, as shown in Fig. 4.5 and Table 4.3. This observation is reversed for propagation along the exterior grain boundary where propagation of the left crack tip requires a higher peak stress and work of separation, as shown in Fig. 4.6 and Table 4.4.

Although trends in the data regarding the traction-separation curves and their corresponding work of separation and peak stress are not as clear for the interior and exterior grain boundaries as they were for the lateral twin grain boundary explored in Chapter 3, some general trends can be gathered. Recall from Section 3.3.2, different random realizations of the same H coverage amount are explored to assess statistical variability in the work of separation and peak stress values for the lateral twin grain boundary. Figure 4.5 and Table 4.2 show that for the interior grain boundaries, as H coverage is increased, the peak stress values remain fairly constant (within the statistical variability), whereas the work of separation is more sensitive to the amount of hydrogen at the grain boundary, increasing by as much as 7.31N/m with 75% of equilibrium coverage for propagation of the left crack tip and decreasing by as much as 13.79N/m for 100% of equilibrium coverage for propagation of the right crack tip, Fig. 4.5 and Table 4.2.

Similarly, the peak stress values for propagation of the right crack tip along the exterior grain boundary remain fairly consistent, well within the variability determined in Section 3.3.2. The effect of hydrogen is most evident in the case of propagation of the left crack tip along the exterior grain boundary where the peak stress decreases by more than 0.7 GPa at all coverages and by as much as 1.36 GPa at 100% of equilibrium coverage, as shown in Figs.4.4, 4.6, and Table 4.3. Figure 4.6 and Table 4.3 also show that propagation of the right crack tip remains fairly consistent with varying coverages of H at the primary grain boundary whereas increasing H coverage lowers the work of separation required for propagation of the left crack tip by more than 9.59 N/m and by as much as 17.17 N/m at 75% of equilibrium coverage.

Due to the lack of clear trends (compared to the lateral twin) in the mechanical response of the interior and exterior systems with the inclusion of increasing amounts of hydrogen at the primary grain boundary, it is suspected that the coverage amounts simulated in this chapter do

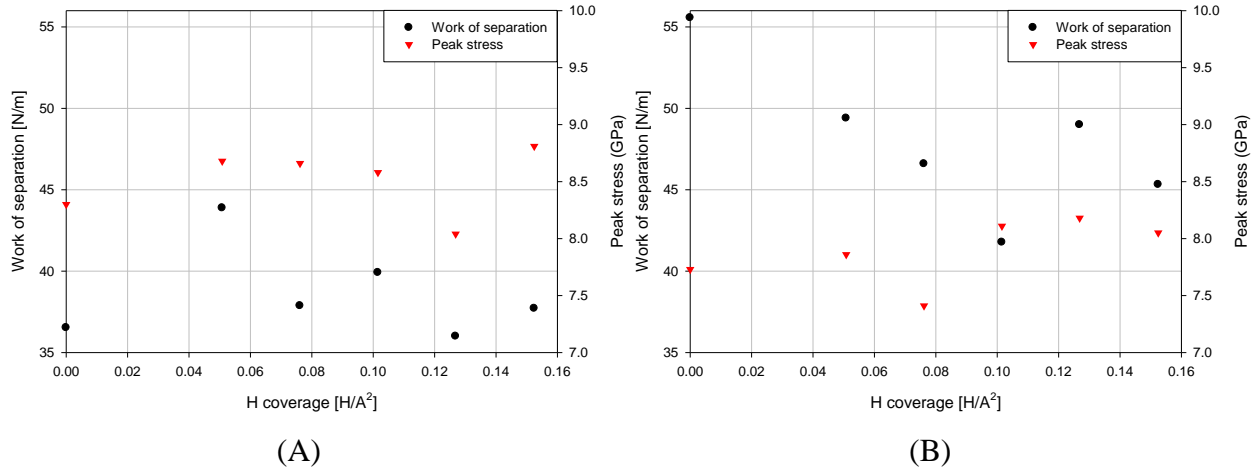


Figure 4.5. Dependence of the work of separation and peak stress as a function of H coverage for propagation of the (A) left (-x direction) and (B) right (+x direction) crack tips in the interior (100.52°) grain boundary system.

	0% H Coverage	50% H Coverage	75% H Coverage	100% H Coverage	125% H Coverage	150% H Coverage
	0.000 H/Å <sup>2</sup>	0.051 H/Å <sup>2</sup>	0.076 H/Å <sup>2</sup>	0.102 H/Å <sup>2</sup>	0.127 H/Å <sup>2</sup>	0.152 H/Å <sup>2</sup>
<b>Left Crack Tip</b>						
Peak Stress [GPa]	8.30	8.68	8.66	8.58	8.04	8.81
Work of Separation [N/m]	36.53	43.84	37.87	39.91	36.00	37.71
<b>Right Crack Tip</b>						
Peak Stress [GPa]	7.73	7.86	7.41	8.11	8.18	8.05
Work of Separation [N/m]	55.56	49.39	46.59	41.77	48.99	45.32

Table 4.2. Peak stress and work of separation for both crack tips at all saturation levels simulated for the interior grain boundary. The peak stress is determined using  $M=250$  running average technique to extract traction-separation relationship and the work of separation is computed using a numerical integration technique.

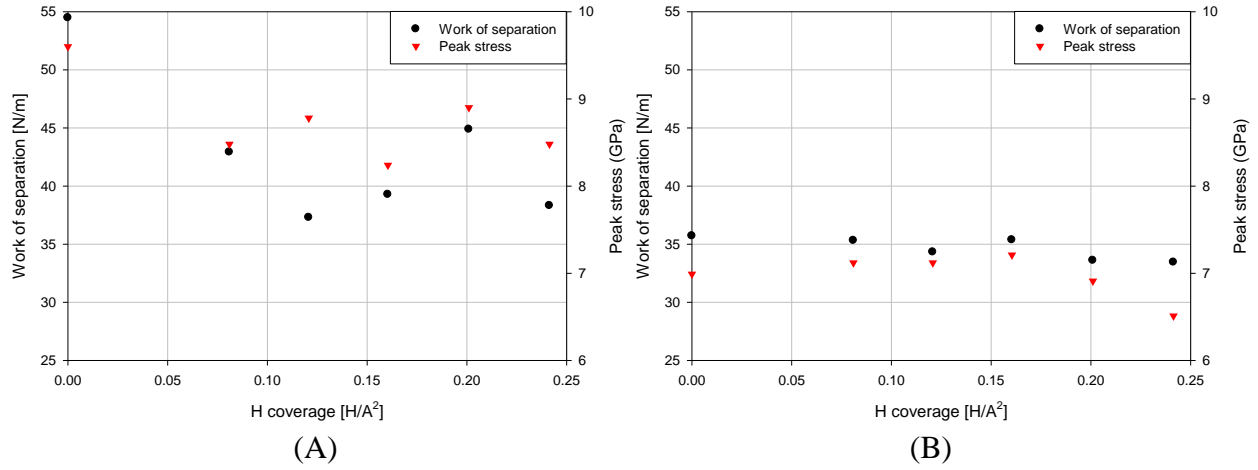


Figure 4.6. Dependence of the work of separation and peak stress as a function of H coverage for propagation of the (A) left (-x direction) and (B) right (+x direction) crack tips in the exterior (119.6°) grain boundary system.

	0% H Coverage	50% H Coverage	75% H Coverage	100% H Coverage	125% H Coverage	150% H Coverage
	0.000 H/Å <sup>2</sup>	0.081 H/Å <sup>2</sup>	0.121 H/Å <sup>2</sup>	0.161 H/Å <sup>2</sup>	0.201 H/Å <sup>2</sup>	0.241 H/Å <sup>2</sup>
<b>Left Crack Tip</b>						
Peak Stress [GPa]	9.60	8.48	8.78	8.24	8.90	8.48
Work of Separation [N/m]	54.47	42.92	37.30	39.28	44.88	38.32
<b>Right Crack Tip</b>						
Peak Stress [GPa]	6.99	7.12	7.12	7.14	7.21	6.91
Work of Separation [N/m]	35.71	35.32	34.32	35.37	33.60	33.45

Table 4.3. Peak stress and work of separation for both crack tips at all saturation levels simulated for the exterior grain boundary. The peak stress is determined using  $M=250$  running average technique to extract traction-separation relationship and the work of separation is computed using a numerical integration technique.

not change the grain boundary structure significantly enough to effect the decohesion mechanisms. This idea is most supported for crack propagation of the right crack tip along the exterior grain boundary where there is no variance outside of the statistical variability, determined in Section 3.3.2, in the work of separation or peak stress with hydrogen coverage. Experiments performed by Lassila and Birnbaum [60,61] indicated that there is a strong dependence of the amount of intergranular fracture (as opposed to ductile fracture) on the amount of hydrogen that is in the system. These experiments, performed on pure polycrystalline Ni [60] and polycrystalline Ni with segregated sulfur [61], showed that increasing the bulk hydrogen concentration dramatically increases the percentage of intergranular fracture, shown in Fig. 4.7. Taking into account the idea of a critical hydrogen concentration resulting in complete intergranular fracture [60,61], it is possible that the coverage amounts of this study are much too low, for these grain boundaries, to result in any increase in brittle fracture. The evidence of a critical hydrogen concentration corresponding to a ductile to brittle transition in single crystal Ni is also supported by coupled atomistic and continuum simulations performed by Song et al. [62] which show that the concentration of hydrogen directly affects the stress intensity,  $K_I$ , necessary to induce cleavage fracture opposed to dislocation emission along certain planes.

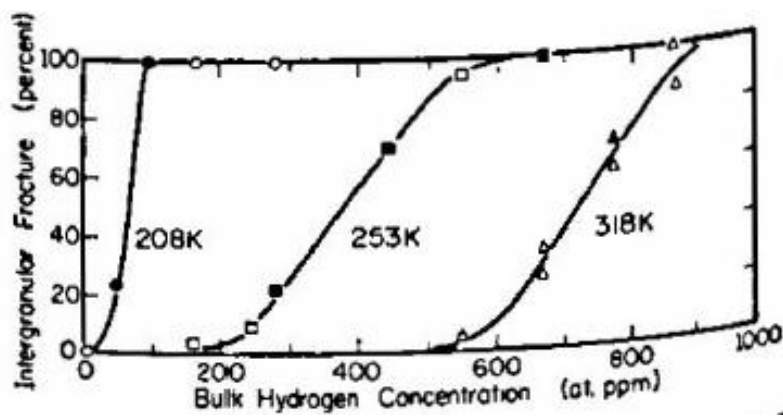


Figure 4.7. Dependence of percentage of intergranular fracture of pure polycrystalline Ni tensile test specimen on the charged bulk hydrogen concentration at three temperatures.[60]

#### 4.5 References

- [42] O'Brien C J and Foiles S M 2014 *Private Communication*
- [60] Lassila D H and Birnbaum H K 1986 The effect of diffusive hydrogen segregation on fracture of polycrystalline nickel *Acta Metall.* **34** 1237–43
- [61] Lassila D H and Birnbaum H K 1987 Intergranular fracture of nickel: the effect of hydrogen-sulfur co-segregation *Acta Metall.* **35** 1815–22
- [62] Song J, Soare M and Curtin W A 2010 Testing continuum concepts for hydrogen embrittlement in metals using atomistics *Model. Simul. Mater. Sci. Eng.* **18** 045003

## CHAPTER 5: CONCLUSIONS

### 5.1 Summary

Recall, there are three main objectives to this thesis: (i) to develop a numerical methodology to extract traction-separation relationships from data obtained through atomistic simulations; (ii) to apply the numerical methodology to specific grain boundaries with different coverages of hydrogen located at the grain boundary interface; (iii) to further the understanding, based on the traction-separation relationships, of the mechanisms by which hydrogen effects the decohesion of a grain boundary. In Chapter 3, a methodology is developed to extract traction-separation relationships and associated material properties from molecular dynamics simulations of steady-state crack propagation along a grain boundary. Sensitivity of the extraction of the traction-separation relationship to the numerical approach is extensively studied as part of Chapter 3. This methodology is used to explore the effects of varying H coverage on the decohesion mechanisms along three grain boundary systems in Ni (the  $\Sigma 3(112)[1\bar{1}0]$  grain boundary in Chapter 3, and two grain boundaries with misorientations interior ( $100.52^\circ$ ) or exterior ( $119.6^\circ$ ) to the  $\Sigma 3(111)[1\bar{1}0]$  symmetric tilt coherent grain boundary in Chapter 4. Six main conclusions can be made as a result of this work.

Regarding the  $\Sigma 3(112)[1\bar{1}0]$  grain boundary system on which the sensitivity of the numerical approach was extensively studied:

1. The traction-separation relationship is dependent on the size of the CVZEs, the number of CZVE that are included in the density of states, and the numerical averaging technique used to derive the cohesive law from  $\rho(\sigma, \lambda)$ .

2. The velocity of the left (-x) crack tip generally increases with increasing H coverage while the velocity of the right (+x) crack tip generally decreases. Such a trend can be associated with a change in the grain boundary structure due to the H coverage and the role of slip system orientation.
3. For crack propagation in both directions, the work of separation generally decreases with increasing H saturation until a minimum is reached around the equilibrium H saturation (in this specific illustration around 66.4% H coverage). Then, the work of separation modestly increases for the oversaturated H coverage.
4. The peak stress during decohesion decreases with increasing H concentration (with the exception of the 50% saturation for the particular primary grain boundary studied). The peak stress in all systems with H is less than the pure Ni system by between 0.51-1.33GPa for propagation of the left crack tip and 0.79-1.67GPa for propagation of the right crack tip.

Regarding the grain boundaries with misorientations interior or exterior to the  $\Sigma 3(111)[1\bar{1}0]$  symmetric tilt coherent grain boundary:

5. With only minor adjustments to the simulation setup parameters for steady-state crack growth, the developed traction-separation methodology can be successfully applied to any grain boundary system with varying amounts of hydrogen segregated to the grain boundary.
6. Although clear trends are not easily attainable from the extracted data regarding the peak stress and work of separation for both near-vicinal twin grain boundary models, it is clear that the inclusion of hydrogen at the grain boundaries does tend to lower the required



work of separation, with the exception of the crack propagation of the left crack tip in the interior ( $100.52^\circ$ ) grain boundary system.

## 5.2 Recommendations for Future Work

Future work should continue to elucidate the embrittlement mechanisms caused by H in Ni using the outlined methodology to extract the traction-separation relationships from a wide range of grain boundaries, including those with both tilt and twist character. As shown in this work, the interplay between hydrogen-induced mechanisms such as HID and HELP, and the structure of the grain boundary relative to the lattice crystallography, is a critical aspect of hydrogen embrittlement that is currently unresolved. Future work will attempt to characterize the defects nucleating from the crack tips and relate the defects to the embrittlement mechanisms experienced. The idea of a critical hydrogen concentration that results in complete brittle or intergranular fracture should also be explored.